A metamaterial consisting of an acoustic black hole plate with local resonators for broadband vibration reduction

Jie Deng, Oriol Guasch, Laurent Maxit, Nansha Gao

A metamaterial consisting of an acoustic black hole plate with local resonators for broadband vibration reduction

Jie Deng[a,*], Oriol Guasch[b], Laurent Maxit[c], Nansha Gao[a,**]

[a]*Key Laboratory of Ocean Acoustic and Sensing, School of Marine Science and Technology, Northwestern Polytechnical University, Xian 710072, China*
[b]*GTM - Grup de Recerca en Tecnologies Mèdia, La Salle, Universitat Ramon Llull C/ Quatre Camins 30, 08022 Barcelona, Catalonia (Spain)*
[c]*INSALyon, Laboratoire Vibrations-Acoustique (LVA) 25 bis, av. Jean Capelle, F-69621 Villeurbanne Cedex, France*

Abstract

Acoustic black hole (ABH) indentations on plates are very efficient to reduce high frequency vibrations. However, when the wavelength of the impinging bending waves on the ABH is larger than its diameter, waves cannot be trapped and dissipated within the ABH and that becomes ineffective. Therefore, it would be highly desirable to extend the performance of ABH plates to lower frequencies. In this work, a method is proposed to accomplish that goal. It is suggested to design a metamaterial in which a set of periodic local resonators are attached to an ABH plate. On the one hand, the resonators are tuned to have a bandgap at the plate first eigenmode so as to suppress it. On the other hand, the resonators are also damped which substantially lowers the peaks of the remaining low-order eigenfrequencies. In combination with the ABH effect, such design, hereafter termed the MMABH plate, provides broadband vibration reduction covering the whole frequency range. To characterize the MMABH, the Gaussian expansion method (GEM) for determining the vibrations of the ABH plate is integrated with a component mode synthesis (CMS) approach, which allows one to link the resonators to the plate. That method is validated against finite element simulations. The MMABH is designed so that its overall mass (ABH plate plus resonators) equals that of the uniform plate without ABH indentation, to offer a light-weight solution. Theoretical explanations of the functioning of the MMABH plate are provided based on the analysis of the ABH effect, the dispersion curves and bandgaps of infinite periodic plates with local resonators and finally, the merging of both topics.

Keywords: Acoustic black holes, Metamaterials, Low frequency, Gaussian expansion, Component mode synthesis

1. Introduction

Research on acoustic black holes (ABHs) in mechanics has experienced a tremendous growth in the past two decades [1]. Most ABHs rely on the variation of the thickness of a structure in such a way that when elastic waves enter the ABH their phase and group velocity diminishes as their amplitude increases. The waves get trapped inside the ABH and their energy is dissipated by means of some damping mechanism (typically a viscoelastic layer is glued at the central region of the ABH). The ABH therefore constitutes a passive, lightweight and efficient way to reduce structural vibrations and sound radiation. Since the initial designs consisting in wedges following a power-law decay thickness at the end of a beam [2–4] and circular [5–8] or groove [9] indentations on plates, several new proposals have been suggested. These include spiral ABHs for beam terminations [10, 11], periodic ABHs embedded in straight [12] and circular beams [13], ABHs on

*Corresponding Author: dengjie@nwpu.edu.cn
**Corresponding Author: gaonansha@nwpu.edu.cn

elliptical plates [14], double-leaf ABHs in plates [12, 15], ring-shaped ABHs for vibration isolation [16, 17] and annular ABHs for cylindrical shells [18–20]. It is worth mentioning that the ABH effect has been also investigated for wave manipulation (see e.g., [21–25] among others), though this topic is out of the scope of this paper.

Most of the above mentioned ABH designs share a common aspect. While being very effective to dissipate vibrations at high frequencies, they fail to do so at low frequencies. In other words, there is a cut-on frequency, $f_{\mathrm{cut-on}}$, beyond which the ABH effect becomes operative, but below which no improvement is found (see e.g., [6]). In a nutshell, the reason for that is as follows. If the wavelength of the impinging waves is larger than the ABH diameter, $2r_{\mathrm{abh}}$, the ABH effect cannot take place as the whole plate essentially vibrates in a combination of global plate modes. The wavelength of the entering waves need to be smaller than the ABH diameter for the waves to slow down and concentrate at its center, where they can be dissipated. Therefore, the radius r_{abh} determines the cut-on frequency $f_{\mathrm{cut-on}}$. In fact, the situation is slightly more intricate because there is a second cut-on frequency, the smoothness one, which guarantees a proper impedance mismatch for waves getting into the ABH (we will not address this issue herein though, see e.g., [26] for details).

To date, only a few strategies have been proposed to improve the performance of ABHs in the lower frequency range. The topic is rather new. On the one hand, some current research has focused in optimizing the ABH profile and the configuration of the damping layers [27]. For instance, adding a platform at the ABH termination enhances its low frequency performance to some extent [28]. Also, multi-objective optimization [29–31] and data-driven schemes [32] have been proposed to modify the ABH thickness profile and achieve a better overall frequency response. However, the most promising strategies for broadband vibration reduction are based on combining the ABH effect with some other technique relying on different background physics, that could be effective at low frequencies. The degree of interaction between the ABH and the low frequency technique is usually not known a priori and whether the coupling would be strong or weak may determine broadband efficiency, design and ease of implementation. One tested option in this line is that of exploiting non-linearity to transfer energy from low to high frequencies, where the ABH becomes efficient. The effects of geometrical [33], material [34], and contact [35, 36] non-linearity have been investigated and experiments have been recently reported in [37]. Using functionally graded [38] and composite [39] materials to build ABH plates has revealed also beneficial. Besides, it has been proved that inserting co-polymers at the entrance and exit of ABHs in beams can also reduce low frequency vibrations [40]. Another approach has involved using ABHs as tuned mass dampers for uniform plates [41, 42]. If the dynamic damper is properly designed to meet, for instance, the critical coupling condition [43–45], the vibration peaks of the host structure below the cut-on frequency can be greatly reduced. In this sense, it is also worthwhile mentioning that tuned absorbers have been also proposed to achieve multimodal vibration reduction in plates [46]. Very recently, a plate comprising periodically tangled ABH cells has been proved very effective for broadband vibration [21] and sound radiation [47] reduction. First steps investigating the performance of non-local ABH structures have also been carried out [48].

On the other hand, in recent years the possibility of suppressing low frequency vibration in structures has also attracted much attention from the field of acoustic metamaterials. Such metamaterials generally involve the arrangement of sub-wavelength material designs periodically or randomly distributed on a host structure. In particular, locally resonant [49] acoustic metamaterials with periodic resonators have been extensively studied for vibration reduction [50–52], sound suppression [53–55], and wave manipulation [56, 57]. Nevertheless, the frequency bandgaps that can be achieved with locally resonant metamaterials are usually very narrow. Despite careful designs have been recently proposed (see e.g., [58, 59] among many others), broadband frequency performance of metamaterials is still a challenge.

This paper presents two contributions. The first one is to propose a metamaterial plate (metaplate) that provides substantial vibration reduction for the whole frequency band, from lower to higher frequencies. To that purpose we consider an ABH plate with a circular indentation and grasp ideas from locally resonant metamaterials to improve its low frequency behavior. For brevity, we will hereafter refer to that plate as the MMABH plate. The strategy we follow is to attach periodic local resonators on the flat side of the ABH plate. The resonators are tuned so as to get a bandgap that suppresses the first ABH plate eigenmode, which is the most energetic one. The resonators become also damped which significantly diminishes the

peak values of all the other low-order plate eigenfrequencies (see e.g., [60–63]). Although the research on locally resonant metamaterials is extensive, as far as the authors know they have not been set yet on ABH plates. Given the change in thickness of the ABH plate it is not clear a priori how the resonators and the ABH plate will interact. Such issue plus other ones will be investigated in this work. It is to be mentioned that a particularity of the proposed MMABH plate is that the mass removed from the uniform plate to make the ABH indentation is recycled as the mass of the resonators. Therefore, no weight increment is involved in the MMABH as compared to the original uniform plate.

The second contribution of this paper concerns the semi-analytical method used to characterize the MMABH plate. It is herein proposed to use the Gaussian expansion method (GEM) in the Rayleigh-Ritz framework previously used to determine the ABH plate vibration field, see [26, 64], and combine it with a component mode synthesis (CMS) approach to link the resonators to the plate. For brevity, and to avoid lengthy labels in the figures, we will refer to that strategy as the GECMS. The GECMS is validated in the paper by comparison with finite element method (FEM) models showing excellent matching, with less computational cost.

The organization of the paper is as follows. In section 2, we first give a brief reminder of the GEM for bare ABH plates and then develop the GECMS method. The efficiency and precision of the GEMCS are compared to those of a FEM model at the end of the section. Section 3 is devoted to characterize the MMABH plate. We start studying its modal behaviour and then present results for the forced case showing the broadband vibration reduction capability of the MMABH. We finish the section with a brief analysis on the MMABH performance depending on the lattice constant. Conclusions close the paper in section 4. Appendix A explains how to apply the GECMS to infinite periodic plates and provides some band gap analysis that becomes useful to better understand the outcomes reported in section 3.

2. Numerical modelling of the MMABH plate

This section focuses on the numerical modelling of the MMABH plate. To that goal, and for completeness, a brief reminder of the Gaussian expansion method (GEM) is first presented to derive the equations of motion of a uniform plate with an embedded circular ABH (see e.g., [26, 64]). Then, the GEM is combined with a component mode synthesis approach to reduce the computational cost and a procedure is established to couple the resonators with the ABH plate. We refer to such modelling method as the GECMS. The GECMS is validated at the end of this section against finite element simulations.

2.1. Gaussian expansion method for an ABH plate

The GEM essentially refers to using Gaussian functions for expanding the displacements of a structure in the framework of the Rayleigh-Ritz method. Let us consider the bending displacement of the ABH plate in Figs. 1a and 1b and express it as the series,

$$w_p(x,y,t) = \sum_{i=1}^{N} a_i(t)\chi_i(x,y) = \boldsymbol{a}^\top(t)\boldsymbol{\chi}(x,y) = \hat{\boldsymbol{A}}^\top \mathrm{e}^{\mathrm{i}\omega t}\boldsymbol{\chi}(x,y), \tag{1}$$

where $\boldsymbol{\chi}(x,y)$ is a vector (with N entries) composed of two-dimensional Gaussian functions, and $\boldsymbol{a}(t) = \hat{\boldsymbol{A}}\mathrm{e}^{\mathrm{i}\omega t}$ represents the time-dependent coefficient vector in harmonic regime.

We can use Eq. (1) to obtain the following expression for the kinetic energy of the ABH plate,

$$\begin{aligned} T_p =& \frac{1}{2}\int_0^{L_y}\int_0^{L_x} \rho_p h(x,y)\dot{w}_p^2 \mathrm{d}x\mathrm{d}y = \frac{1}{2}\int_0^{L_y}\int_0^{L_x} \rho_p h(x,y)\left(\dot{\boldsymbol{a}}^\top\boldsymbol{\chi}\boldsymbol{\chi}^\top\dot{\boldsymbol{a}}\right)\mathrm{d}x\mathrm{d}y \\ =& \frac{1}{2}\dot{\boldsymbol{a}}^\top\left[\int_0^{L_y}\int_0^{L_x} \rho_p h(x,y)\left(\boldsymbol{\chi}\boldsymbol{\chi}^\top\right)\mathrm{d}x\mathrm{d}y\right]\dot{\boldsymbol{a}} \equiv \frac{1}{2}\dot{\boldsymbol{a}}^\top\boldsymbol{M}_p\dot{\boldsymbol{a}}, \end{aligned} \tag{2}$$

where ρ_p stands for the density of the plate and $h(x,y) = \varepsilon r^m + h_c$ for its local thickness. In the last expression, m denotes the ABH order, $r = [(x - L_x/2)^2 + (y - L_y/2)^2]^{1/2}$ the distance to the ABH center,

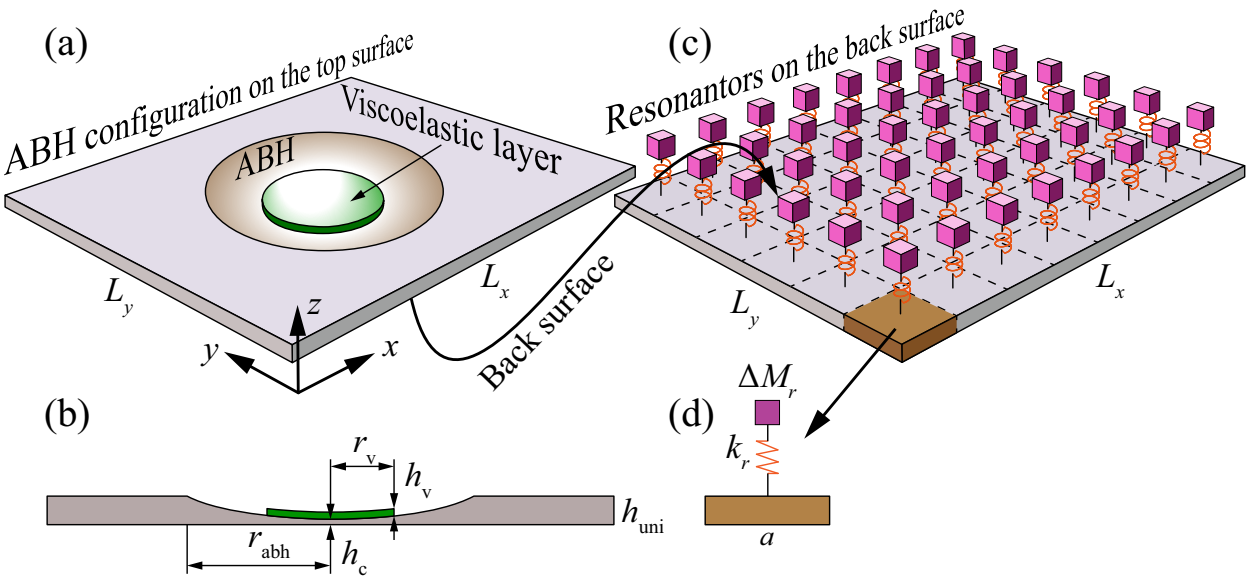

Figure 1: (a) Plate with a circular ABH indentation with a viscoelastic layer on the top surface. (b) ABH plate profile. (c) Configuration of periodic resonators on the bottom surface of the ABH plate. (d) Details of the unit cell.

$\varepsilon = (h_{\text{uni}} - h_c)/r_{\text{abh}}^m$ the slope (also referred to as the smoothness parameter) and h_c the residual thickness at the center of the ABH. In the second row of Eq. (2) we have identified the mass matrix $\boldsymbol{M}_p$.

If we proceed analogously for the potential energy, we get,

$$\begin{aligned} V_p =& \frac{1}{2}\int_0^{L_y}\int_0^{L_x} D_p(x,y)\left[\left(\frac{\partial^2 w_p}{\partial x^2}\right)^2 + \left(\frac{\partial^2 w_p}{\partial y^2}\right)^2\right. \\ &\left. +\nu_p \frac{\partial^2 w_p}{\partial x^2}\frac{\partial^2 w_p}{\partial y^2} + \nu_p \frac{\partial^2 w_p}{\partial y^2}\frac{\partial^2 w_p}{\partial x^2} + 2(1-\nu_p)\left(\frac{\partial^2 w_p}{\partial x \partial y}\right)^2\right] \mathrm{d}x\mathrm{d}y \\ =& \frac{1}{2}\boldsymbol{a}^\top \left\{\int_0^{L_y}\int_0^{L_x} D_p(x,y)\left[\frac{\partial^2 \boldsymbol{\chi}}{\partial x^2}\frac{\partial^2 \boldsymbol{\chi}^\top}{\partial x^2} + \frac{\partial^2 \boldsymbol{\chi}}{\partial y^2}\frac{\partial^2 \boldsymbol{\chi}^\top}{\partial y^2}\right.\right. \\ &\left.\left. +\nu_p \frac{\partial^2 \boldsymbol{\chi}}{\partial x^2}\frac{\partial^2 \boldsymbol{\chi}^\top}{\partial y^2} + \nu_p \frac{\partial^2 \boldsymbol{\chi}}{\partial y^2}\frac{\partial^2 \boldsymbol{\chi}^\top}{\partial x^2} + 2(1-\nu_p)\frac{\partial^2 \boldsymbol{\chi}}{\partial x \partial y}\frac{\partial^2 \boldsymbol{\chi}^\top}{\partial y \partial x}\right] \mathrm{d}x\mathrm{d}y\right\}\boldsymbol{a} \\ \equiv& \frac{1}{2}\boldsymbol{a}^\top \boldsymbol{K}_p \boldsymbol{a}, \end{aligned} \tag{3}$$

where $D_p(x,y) = E_p(1+\mathrm{i}\eta_p)h^3(x,y)/[12(1-\nu_p^2)]$ designates the bending stiffness of the ABH plate, E_p being its Young modulus, η_p the loss factor and ν_p the Poisson ratio. As previously done for the plate mass matrix, in the last line of Eq. (3) we have introduced the stiffness matrix $\boldsymbol{K}_p$. Besides, to dissipate vibration energy we consider a circular viscoelastic layer of thickness h_v and radius r_v placed at the ABH center. The damping layer mass and stiffness matrices can be obtained in the same way as those in Eqs. (2) and (3), assuming the full coupling condition (see [26, 65]). For the sake of exposition these matrices, namely $\boldsymbol{M}_{\text{vis}}$ and $\boldsymbol{K}_{\text{vis}}$ are not shown here (to get them one only needs to respectively replace the Young modulus, density, Poisson ration and loss factor in the expressions for $\boldsymbol{M}_p$ nd $\boldsymbol{K}_p$ by E_v, ρ_v, η_v and η_v). In what follows, and to ease notation, we will assume that $\boldsymbol{M}_p$ and $\boldsymbol{K}_p$ already account for the influence of the damping layer.

On the other hand, the external work resulting from a harmonic point force $F(t) = \hat{F}\mathrm{e}^{\mathrm{i}\omega t}$ exerted at the ABH plate coordinates (x_f, y_f) is given by,

$$W = F(t)w(t,x_f,y_f) = \boldsymbol{a}^\top\left[F(t)\boldsymbol{\chi}(x_f,y_f)\right] \equiv \boldsymbol{a}^\top \boldsymbol{F} = \boldsymbol{a}^\top \hat{\boldsymbol{F}}\mathrm{e}^{\mathrm{i}\omega t}, \tag{4}$$

where we have defined the force vector $\boldsymbol{F} = \hat{\boldsymbol{F}}\mathrm{e}^{\mathrm{i}\omega t}$ in the last equality of Eq. (4).

Combining Eqs. (2)-(4) we can build the Lagrangian of the damped ABH plate,

$$\mathscr{L} = T_p - V_p + W = \frac{1}{2}\dot{\boldsymbol{a}}^\top \boldsymbol{M}_p \dot{\boldsymbol{a}} - \frac{1}{2}\boldsymbol{a}^\top \boldsymbol{K}_p \boldsymbol{a} + \boldsymbol{a}^\top \boldsymbol{F}, \tag{5}$$

and applying the Euler-Lagrange equations $\partial_t(\partial_{\dot{\boldsymbol{a}}}\mathscr{L}) - \partial_{\boldsymbol{a}}\mathscr{L} = \boldsymbol{0}$ to Eq. (5) we get the equations of motion,

$$\left(\boldsymbol{K}_p - \omega^2 \boldsymbol{M}_p\right)\hat{\boldsymbol{A}} = \hat{\boldsymbol{F}}. \tag{6}$$

The solution to Eq. (6) determines how the ABH plate vibrates under the loading of the force vector $\hat{\boldsymbol{F}}$.

2.2. The GECMS method for the MMABH plate

Once seen how to characterize the vibrations of the ABH plate with the GEM in section 2.1, we are in a position to model the performance of the MMABH plate depicted in Fig. 1c.

We begin by setting $\hat{\boldsymbol{F}} = \boldsymbol{0}$ in Eq. (6) and computing the modal matrix $\hat{\boldsymbol{P}} = [\hat{\boldsymbol{A}}_1, \hat{\boldsymbol{A}}_2, \hat{\boldsymbol{A}}_3, ..., \hat{\boldsymbol{A}}_i, ..., \hat{\boldsymbol{A}}_N]$. Then, we reduce the dimensions of the original model by considering the first $\overline{N}$ mass-normalized modal vectors $\overline{\boldsymbol{P}} = [\overline{\boldsymbol{A}}_1, \overline{\boldsymbol{A}}_2, \overline{\boldsymbol{A}}_3, ..., \overline{\boldsymbol{A}}_i, ..., \overline{\boldsymbol{A}}_{\overline{N}}]$, with $\overline{N} \ll N$ and $\overline{\boldsymbol{A}}_i = \hat{\boldsymbol{A}}_i / \sqrt{\hat{\boldsymbol{A}}_i^\top \boldsymbol{M}_p \hat{\boldsymbol{A}}_i}$, $\forall\ i = 1 \dots \overline{N}$. The generalized ABH plate mass and stiffness matrices are obtained as,

$$\begin{aligned} \overline{\boldsymbol{M}}_p &= \overline{\boldsymbol{P}}^\top \boldsymbol{M}_p \overline{\boldsymbol{P}}, \\ \overline{\boldsymbol{K}}_p &= \overline{\boldsymbol{P}}^\top \boldsymbol{K}_p \overline{\boldsymbol{P}}. \end{aligned} \tag{7}$$

By projecting the coefficient vector of Eq. (1) into the modal space we get,

$$\boldsymbol{a} = \overline{\boldsymbol{P}}\boldsymbol{\varepsilon}_p, \tag{8}$$

which once used in the expression for the ABH plate kinetic energy yields,

$$T_p = \frac{1}{2}\dot{\boldsymbol{a}}^\top \boldsymbol{M}_p \dot{\boldsymbol{a}} \equiv \frac{1}{2}\dot{\boldsymbol{\varepsilon}}_p^\top \overline{\boldsymbol{M}}_p \dot{\boldsymbol{\varepsilon}}_p. \tag{9}$$

As done in previous equations, in the last line we have introduced the reduced mass matrix which turns to be the identity matrix as we are using mass-normalized eigenvectors.

On the other hand, let us consider a total of N_r resonators linked to the ABH plate (see Fig. 1c). The kinetic energy of the i-th resonator (Fig. 1d) is given by,

$$T_{ri} = \frac{1}{2}\dot{w}_{ri}\Delta M_{ri}\dot{w}_{ri} = \frac{1}{2}\dot{\overline{w}}_{ri}\dot{\overline{w}}_{ri}, \qquad \forall\, i = 1 \dots N_r, \tag{10}$$

where $\overline{w}_{ri} = w_{ri}/\sqrt{\Delta M_{ri}}$. The total kinetic energy of the MMABH plate can thus be computed as,

$$
\begin{aligned}
T &= T_p + \sum_{i=1}^{N_r} T_{ri} \\
&= \frac{1}{2}\dot{\boldsymbol{\varepsilon}}_p^\top \overline{\boldsymbol{M}}_p \dot{\boldsymbol{\varepsilon}}_p + \sum_{i=1}^{N_r} \frac{1}{2}\dot{\overline{w}}_{ri}\dot{\overline{w}}_{ri} \\
&= \frac{1}{2}\begin{bmatrix} \dot{\boldsymbol{\varepsilon}}_p \\ \dot{\overline{w}}_{r1} \\ \dot{\overline{w}}_{r2} \\ \dot{\overline{w}}_{r3} \\ \vdots \\ \dot{\overline{w}}_{ri} \\ \vdots \\ \dot{\overline{w}}_{rN_r} \end{bmatrix}^\top \begin{bmatrix} \overline{\boldsymbol{M}}_p & \mathbf{0} & \mathbf{0} & \mathbf{0} & \cdots & \mathbf{0} & \cdots & \mathbf{0} \\ \mathbf{0} & 1 & 0 & 0 & \cdots & 0 & \cdots & 0 \\ \mathbf{0} & 0 & 1 & 0 & \cdots & 0 & \cdots & 0 \\ \mathbf{0} & 0 & 0 & 1 & \cdots & 0 & \cdots & 0 \\ \vdots & \vdots & \vdots & \vdots & \ddots & \vdots & \ddots & \vdots \\ \mathbf{0} & 0 & 0 & 0 & \cdots & 1 & \cdots & 0 \\ \vdots & \vdots & \vdots & \vdots & \ddots & \vdots & \ddots & \vdots \\ \mathbf{0} & 0 & 0 & 0 & \cdots & 0 & \cdots & 1 \end{bmatrix} \begin{bmatrix} \dot{\boldsymbol{\varepsilon}}_p \\ \dot{\overline{w}}_{r1} \\ \dot{\overline{w}}_{r2} \\ \dot{\overline{w}}_{r3} \\ \vdots \\ \dot{\overline{w}}_{ri} \\ \vdots \\ \dot{\overline{w}}_{rN_r} \end{bmatrix} \\
&\equiv \frac{1}{2}\dot{\boldsymbol{\varepsilon}}^\top \widetilde{\boldsymbol{M}} \dot{\boldsymbol{\varepsilon}}.
\end{aligned} \tag{11}
$$

Likewise, the potential energy stored in the i-th spring is

$$
\begin{aligned}
V_{ri} &= \frac{1}{2}k_r \left[w_p(x_{ci}, y_{ci}) - w_{ri}\right]^2 \\
&= \frac{1}{2}k_r \left[w_p^2(x_{ci}, y_{ci}) - w_p(x_{ci}, y_{ci})w_{ri} - w_{ri}w_p(x_{ci}, y_{ci}) + w_{ri}^2\right] \\
&= \frac{1}{2}\begin{bmatrix} \boldsymbol{\varepsilon}_p \\ \overline{w}_{ri} \end{bmatrix}^\top \left(\begin{bmatrix} \overline{\boldsymbol{P}} & \mathbf{0} \\ \mathbf{0} & 1 \end{bmatrix}^\top \begin{bmatrix} k_r \boldsymbol{\chi}_i \boldsymbol{\chi}_i^\top & -k_r \boldsymbol{\chi}_i \\ -k_r \boldsymbol{\chi}_i^\top & \omega_r^2 \end{bmatrix} \begin{bmatrix} \overline{\boldsymbol{P}} & \mathbf{0} \\ \mathbf{0} & 1 \end{bmatrix} \right) \begin{bmatrix} \boldsymbol{\varepsilon}_p \\ \overline{w}_{ri} \end{bmatrix} \\
&\equiv \frac{1}{2}{\boldsymbol{\varepsilon}_i}^\top \overline{\boldsymbol{K}}_{ri} \boldsymbol{\varepsilon}_i, \qquad \forall\, i = 1 \ldots N_r,
\end{aligned} \tag{12}
$$

where $\boldsymbol{\chi}_i = \boldsymbol{\chi}(x_{ci}, y_{ci})$ stands for the shape function vector at the location (x_i, y_i) of the i-th resonator.

Geometry parameters	Material parameters
$m = 2.5$	$\rho_p = 7800$ kg/m^3
$L_x = 0.8$ m	$E_p = 210$ GPa
$L_y = 0.6$ m	$\eta_p = 0.01$
$h_{uni} = 0.005$ m	$\nu_p = 0.3$
$r_{abh} = 0.24$ m	
$\varepsilon = 0.1595$ m$^{-1.5}$	$\rho_v = 950$ kg/m^3
$h_c = 0.0005$ m	$E_v = 5$ GPa
$r_v = 0.12$ m	$\eta_v = 0.5$
$h_v = 0.0005$ m	$\nu_v = 0.3$

Table 1: Geometrical and material parameters of the ABH plate. ρ_p: plate density, ρ_v: damping layer density, E_p: plate Young modulus, E_v: damping layer Young modulus, η_p: plate loss factor, η_v: damping layer loss factor, ν_p: plate Poisson ratio, ν_v: damping layer Poisson ratio.

Considering Eq. (12), the total potential energy of the MMABH plate becomes

$$
\begin{aligned}
V &= V_p + \sum_{i=1}^{N_r} V_{ri} \\
&= \frac{1}{2}\boldsymbol{\varepsilon}_p^{\top}\overline{\boldsymbol{K}}_p\boldsymbol{\varepsilon}_p + \sum_{i=1}^{N_r}\frac{1}{2}{\boldsymbol{\varepsilon}_i}^{\top}\overline{\boldsymbol{K}}_{ri}\boldsymbol{\varepsilon}_i \\
&\equiv \frac{1}{2}\begin{bmatrix} \boldsymbol{\varepsilon}_p \\ \overline{w}_{r1} \\ \overline{w}_{r2} \\ \overline{w}_{r3} \\ \vdots \\ \overline{w}_{ri} \\ \vdots \\ \overline{w}_{rN_r} \end{bmatrix}^{\top} \left(\widetilde{\boldsymbol{P}}^{\top}\widetilde{\boldsymbol{K}}\widetilde{\boldsymbol{P}}\right) \begin{bmatrix} \boldsymbol{\varepsilon}_p \\ \overline{w}_{r1} \\ \overline{w}_{r2} \\ \overline{w}_{r3} \\ \vdots \\ \overline{w}_{ri} \\ \vdots \\ \overline{w}_{rN_r} \end{bmatrix} \\
&\equiv \frac{1}{2}\boldsymbol{\varepsilon}^{\top}\overline{\boldsymbol{K}}\boldsymbol{\varepsilon},
\end{aligned} \tag{13}
$$

where

$$
\widetilde{\boldsymbol{P}} = \operatorname{diag}\left(\overline{\boldsymbol{P}}, \overbrace{1,1,1,\ldots,1}^{N_r}\right), \tag{14}
$$

$$
\widetilde{\boldsymbol{K}} = \begin{bmatrix}
\overline{\boldsymbol{K}}_p + k_r\sum_{i=1}^{N_r}\boldsymbol{\chi}_i\boldsymbol{\chi}_i^{\top} & -k_r\boldsymbol{\chi}_1 & -k_r\boldsymbol{\chi}_2 & -k_r\boldsymbol{\chi}_3 & \cdots & -k_r\boldsymbol{\chi}_i & \cdots & -k_r\boldsymbol{\chi}_{N_r} \\
-k_r\boldsymbol{\chi}_1^{\top} & \omega_r^2 & 0 & 0 & \cdots & 0 & \cdots & 0 \\
-k_r\boldsymbol{\chi}_2^{\top} & 0 & \omega_r^2 & 0 & \cdots & 0 & \cdots & 0 \\
-k_r\boldsymbol{\chi}_3^{\top} & 0 & 0 & \omega_r^2 & \cdots & 0 & \cdots & 0 \\
\vdots & \vdots & \vdots & \vdots & \ddots & \vdots & \ddots & \vdots \\
-k_r\boldsymbol{\chi}_i^{\top} & 0 & 0 & 0 & \cdots & \omega_r^2 & \cdots & 0 \\
\vdots & \vdots & \vdots & \vdots & \ddots & \vdots & \ddots & \vdots \\
-k_r\boldsymbol{\chi}_{N_r}^{\top} & 0 & 0 & 0 & \cdots & 0 & \cdots & \omega_r^2
\end{bmatrix}. \tag{15}
$$

Finally, applying the Euler-Lagrange equations to Eqs. (9)-(15) and assuming $\boldsymbol{\varepsilon} = \hat{\boldsymbol{\varepsilon}}\exp(\mathrm{i}\omega t)$, we derive the eigenvalue problem

$$
\left(\widetilde{\boldsymbol{K}} - \omega^2\widetilde{\boldsymbol{M}}\right)\hat{\boldsymbol{\varepsilon}} = \mathbf{0}, \tag{16}
$$

from which the synthesized modes of the MMABH plate can be calculated.

2.3. Validity of the GECMS method to simulate the MMABH plate

The efficiency and accuracy of the GECMS developed in the previous section is next validated against FEM simulations. Prior to that, however, let us introduce some significant details on the configuration of the MMABH plate. As explained before, our suggestion to extend the performance of the ABH plate to lower frequencies relies on attaching a periodic arrangement of local resonators to the bottom surface of the

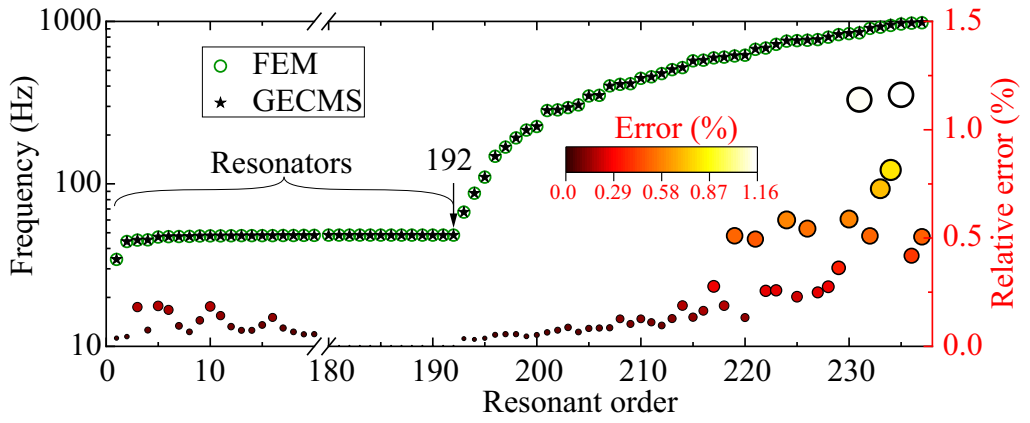

Figure 2: Comparison of eigenfrequencies computed with GECMS and FEM, together with their relative error percentage that is symbolized by the size and color of the bubbles. Note there is a break range between the resonant orders 20 and 180.

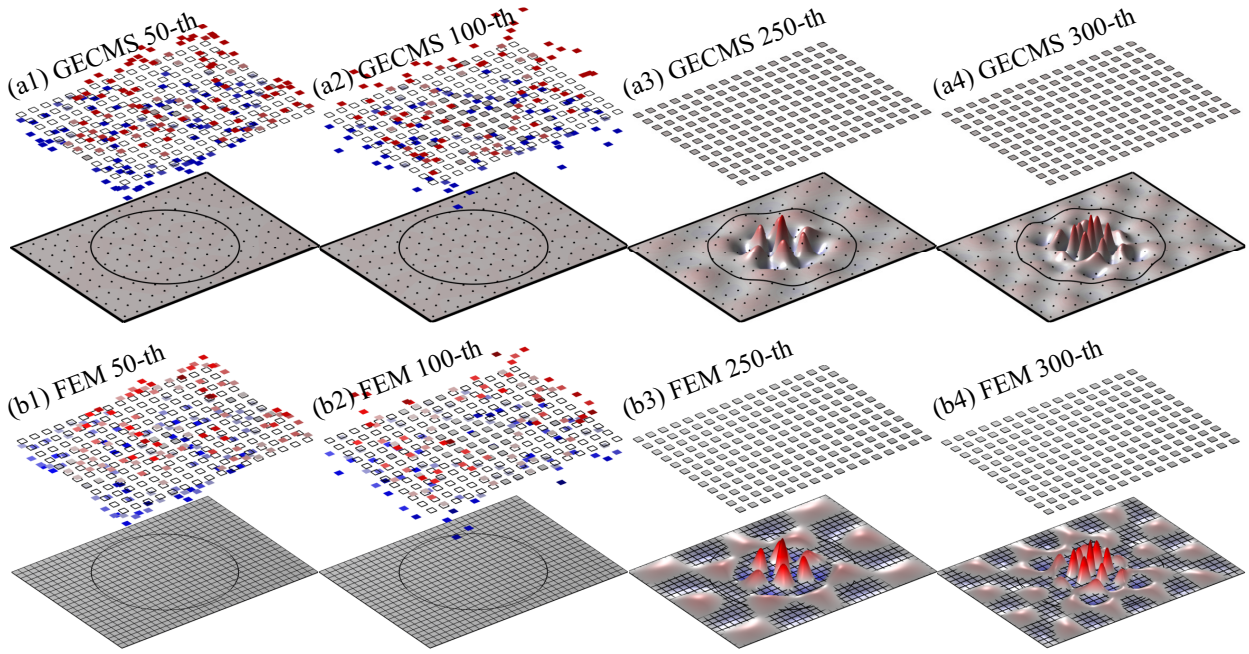

Figure 3: Modal shapes computed with (a) GECMS and (b) FEM.

ABH plate (see Fig. 1c). For the sake of light-weight design and fair comparison, the mass removed from the plate when manufacturing the ABH indentation is recycled to constitute the mass of the resonators. According to the geometrical and material parameters in Table 1, the mass extracted from the uniform plate is given by $\Delta M = \rho_p L_x L_y h_{\text{uni}} - \rho_p \int_0^{L_x} \int_0^{L_y} h(x,y)\mathrm{d}y\mathrm{d}x = 3.5286$ kg. We evenly distribute ΔM among $N_r = 192$ resonators, which are located at the centers of the cells resulting from respectively partitioning L_x and L_y into 16 and 12 equal segments. The lattice constant of the MMABH plate is therefore $a = 0.05$ m (square lattice). As a consequence, the mass of each resonator becomes $\Delta M_r = 0.0184$ kg. Because the ABH plate's first eigenfrequency is $f_1 = 48.3$ Hz, we tune the resonators to that frequency, which results in a stiffness value of the springs of $k_r = (2\pi f_r)^2 \Delta M_r = 1692.6$ N/m. Simply supported boundary conditions are considered at the four edges of the plate.

As regards the FEM model, it was built using the commercial software COMSOL Multiphysics. The

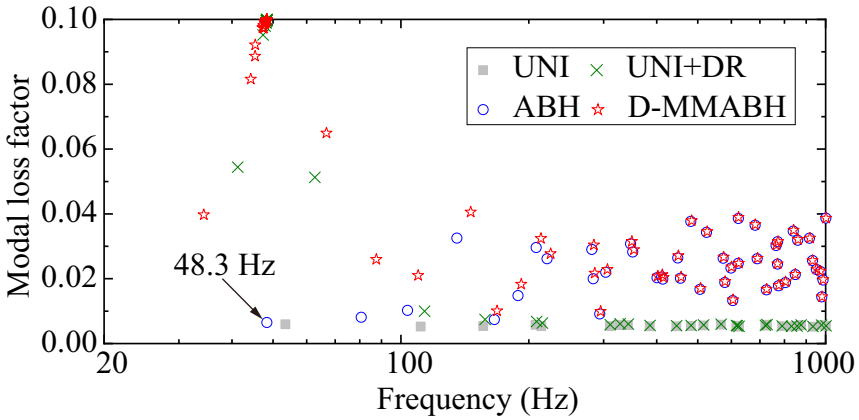

Figure 4: Comparison of the modal loss factors (MLFs) for a uniform plate (UNI), an ABH plate (ABH) a uniform plate with damped resonators (UNI+DR) and the MMABH plate with damped resonators (D-MMABH).

3D *Shell* module was employed to simulate the ABH plate by defining a local thickness, and the springs were introduced via a virtual *Spring-Damper* option, with the spring ends connecting the center of each cell and the mass of the resonator. The in-plane vibrations were not considered to reduce the number of degrees of freedom (dofs). The FEM model consisted of 854 triangular and 26724 quadrilateral elements, involving a total of 615246 dofs. The GEM model for the ABH plate, however, only required $N = 2714$ two-dimensional Gaussian basis functions implying a total of $N = 2714$ dofs. The modal decomposition allowed us to further reduce the GEM model by a factor of ten (i.e., $\overline{N} \approx N/10$) as only the first $\overline{N} = 272$ modes were necessary for the analyzed frequency range. Note that modal frequency of the 272-nd mode is 9486 Hz, which is much larger than 1000 Hz, which is the highest frequency of interest. After connecting the 192 resonators to the ABH plate, the total dofs of the GECMS became 464, which are much less than the FEM model ones. Note that FEM requires a very fine mesh to correctly capture the vibrations at the center of the ABH, because the thickness there is very thin. In what concerns the computational cost, it only took 10 seconds to calculate the MMABH plate response with the GECMS by sweeping the frequency from 20 Hz to 1000 Hz with a resolution of 0.1 Hz, on a personal computer AMD 5950X. In contrast, the FEM computation took 49 hours to solve the same problem. By comparing the running times we can see the advantages of the proposed GECMS method.

Once shown the computational efficiency of the GECMS, we focus on its accuracy. The modal frequencies of the MMABH computed with the GECMS (blue dots) and FEM (black stars) have been depicted for comparison in Fig. 2. For an easier inspection, there is a break in the abscissa of the plot between the 20-th and 180-th orders and the frequency axis is represented in a logarithmic scale. The matching between the GECMS and FEM is remarkable. The relative error (see the right axis in Fig. 2), $\varepsilon^f_{\text{rel}} \equiv |f_{\text{FEM}} - f_{\text{GECMS}}|/f_{\text{FEM}} \times 100\%$, has been computed and represented by the color and size of the circles in the figure. For the first 192 orders $\varepsilon^f_{\text{rel}}$ is no greater than 0.18% and beyond them it does not surpass 1.16%. In addition, the modal shapes of the 50-th, 100-th, 250-th and 300-th orders are illustrated in Fig. 3 using both methods; the first row corresponding to the GECMS and the second one to the FEM. The small squares in the upper layers of the figure symbolize the resonators. In Fig. 3a, the points on the plate indicate the coupling locations. Once more, the GECMS and FEM results look very similar, validating the precision of the former. We elaborate more on the modal shapes of the MMABH plate below.

3. Performance of the MMABH plate

3.1. Modal behaviour of the MMABH plate

After validating the GECMS model, we next inspect the modal behaviour of the MMABH plate to understand how the damping distributes within modes and how the local resonances interact with the

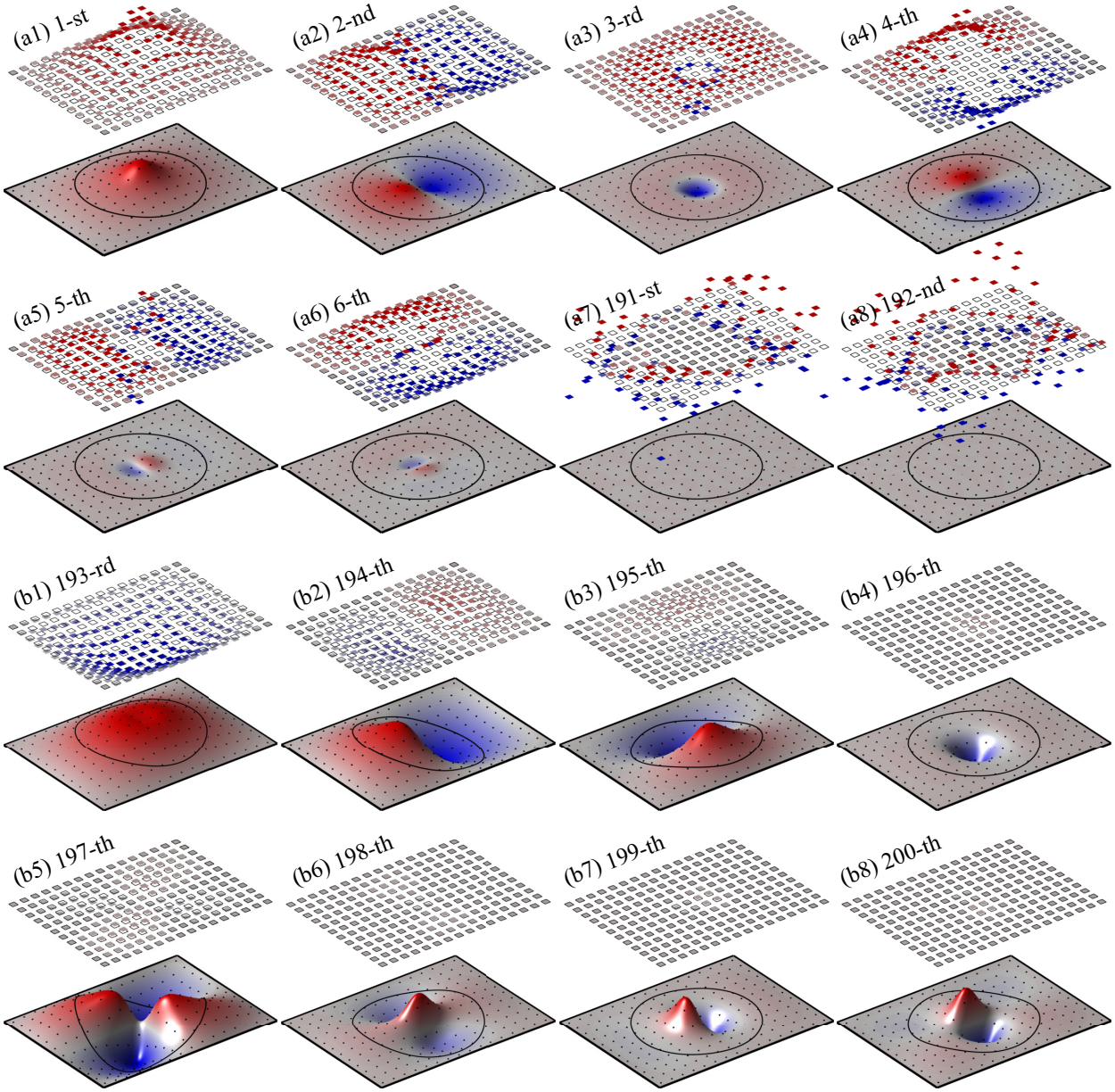

Figure 5: Modal shapes of the MMABH plate. (a1)-(a8) associate with the modal order no greater than 192, while (b1)-(b8) correlate to the ones higher than 192.

ABH effect. Starting with the former, Fig. 4 presents the modal loss factors (MLFs) computed for four different plates: a uniform plate (UNI), an ABH plate (ABH), a uniform plate with damped local resonators (UNI+DR) and the MMABH plate (MMABH). It is seen that for the uniform (UNI) plate the MLF is constant and equal to 0.005 for all modes. When including resonators with loss factor $\eta_r = 0.1$ to the uniform plate, the MLFs of the modes close to the plate's first eigenfrequency $f_1 = 48.3$ Hz increase, though no changes are appreciated for higher order modes. This is reasonable since the resonators were tuned to act on f_1. The situation is very different for the ABH plate. In this case, large MLFs are expected at the higher frequencies due to the ABH effect, and this is what is observed in the figure for $f \gtrsim 200$ Hz (compare with the UNI case). However, it is seen that the ABH plate MLFs at lower orders are very small, especially

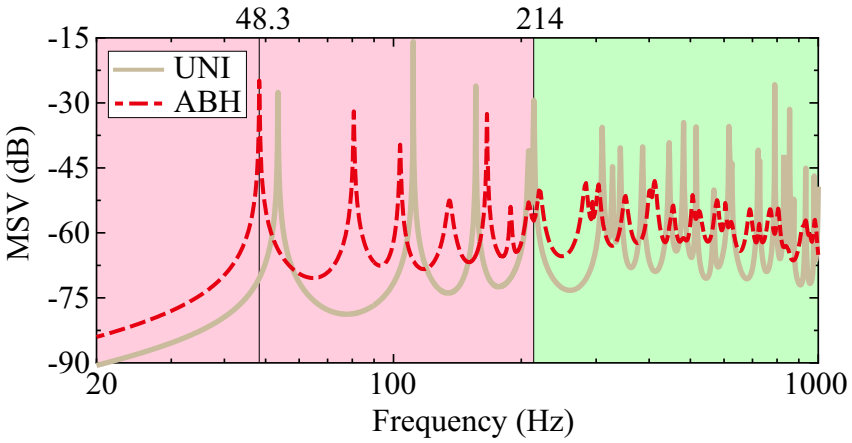

Figure 6: Mean square velocity (MSV) comparison between the ABH plate and the uniform (UNI) one. For frequencies beyond the diameter cut-on frequency the ABH effect performs well (light green shaded region), but in the lower frequency range the ABH behavior can become worse than that of a uniform plate (light red shaded area).

at f_1. This is solved to a large extent by adding damped resonators to the ABH plate to build the MMABH. Significant MLFs are then obtained for the whole frequency range.

Let us next have a look at the modal shapes of the MMABH plate to inspect how the resonators interact with the ABH plate (see Fig. 5). The first two rows of the figure, namely (a1-a8), correspond to modal shapes whose orders are lower than or equal to 192. For the 1-st order (see Fig. 5a1), we observe that the ABH plate vibrates in phase with the resonators and with similar amplitude. This indicates that the effective mass of the whole structure is greater than the real one (see e.g., [59, 60], among others). As the modal order increases, the vibration amplitude of the resonators augments while that of the plate diminishes. This holds true up to the 192-nd order at which the amplitude of the resonators becomes maximum, whereas the ABH plate exhibits almost no motion. Also, the effective mass gets its highest value. However, once past the 192-nd order the behaviour of the MMABH totally changes. For the 193-rd one (see Fig. 5b1), the ABH plate starts vibrating again but with opposite phase to the resonators, which results in small or even negative effective mass. As the modal order keeps increasing, the resonators become static and the plate exhibits strong vibrations, especially in the ABH central area (see Figs. 5b1-5b8). These phenomena can also be appreciated in the previous Fig. 3, which we used to compare GECMS and FEM simulations.

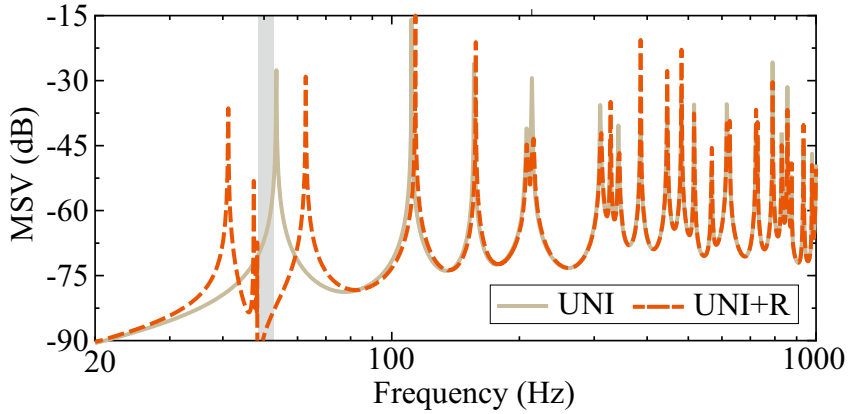

Figure 7: Mean square velocity (MSV) comparison of the uniform (UNI) plate with and without non-damped resonators (R).

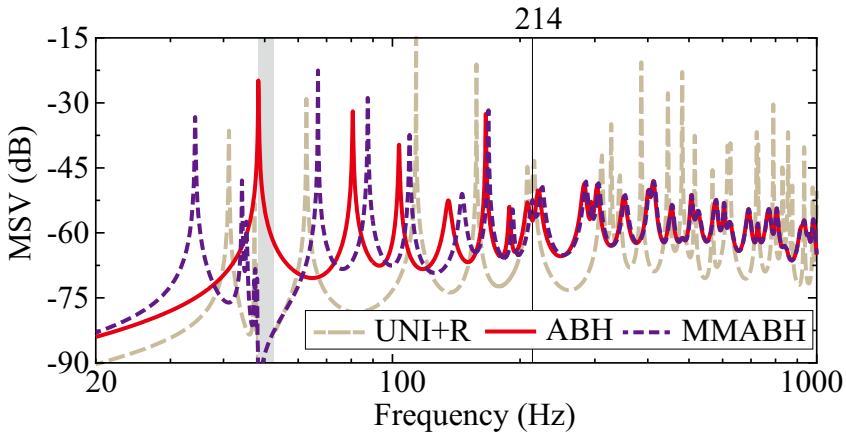

Figure 8: Mean square velocity (MSV) comparison of the bare ABH plate (ABH) and the MMABH plate with non-damped resonators (MMABH).

3.2. Broadband vibration reduction of the MMABH plate under external force

We now turn our attention to the MMABH plate response when excited by an external point force $\hat{F}$. This is assumed to be 1 N in amplitude for all frequencies, perpendicularly pointing towards the plate and located at $(x_f, y_f) = (0.7, 0.5)$ m. To characterize the plate response we compute its mean square velocity (MSV), MSV (dB)=$10\log\left[\int_0^{L_x}\int_0^{L_y}\omega^2 w^2(x,y)\mathrm{d}y\mathrm{d}x/(L_xL_y)\right]$, when submitted to $\hat{F}$.

According to the values in Table 1, the embedded ABH has a radius $r_{abh} = 0.24$ m, so its associated diameter cut-on frequency becomes $f_{\mathrm{cut-on}} = \frac{\pi h_{\mathrm{uni}}}{4r_{\mathrm{abh}}^2}\sqrt{\frac{E_p}{3\rho(1-\nu_p^2)}}$=214 Hz. It is therefore expected that beyond 214 Hz the ABH effect will take place and vibrations will considerably diminish. As the response of a single ABH plate under external excitation is well-known and has been extensively studied in the specialized literature (see e.g., [1, 5–7, 26] among others), we will not address this issue in detail below. We simply present in Fig. 6, a comparison between the MSV of a uniform plate (UNI) of thickness h_{uni} with that of the ABH plate (ABH). The uniform plate has the same amount of damping layer than the ABH one for a fair comparison. As expected, the ABH substantially reduces the MSV for frequencies higher than 214 Hz (region shaded in light green color). However, for lower frequencies the ABH is totally inefficient (area shaded in light red). In particular, the stiffness reduction due to the ABH indentation even worsens the response of the ABH plate with respect to the uniform one. This is very obvious for the first resonant frequency of the uniform plate, $f_1 = 48.3$ Hz.

On the other hand, once we add the resonators to the ABH plate to build the MMABH metaplate band gaps appear and one would expect to somewhat broaden the vibration reduction to lower frequencies. Once more, given that the underlying physics of adding resonators to uniform plates have been also widely discussed in literature (see e.g., [60–63], among others) we will not address that issue below, but mostly focus on the MMABH plate. We refer the reader to Appendix A to see how to compute the dispersion curves of infinite periodic uniform plates with resonators using the GECMS method, and for results concerning the band gaps dependence on the lattice constant and plate thickness of a uniform plate having the resonators of the present case. Nevertheless, for comparison purposes with the performance of the MMABH plate, it is interesting to show in Fig. 7 the effects of the resonators on the uniform plate (UNI) also depicted in Fig. 6. Fig. 7 reveals that the MSV of the (UNI+R) plate strongly diminishes within the bandgap (shaded in gray) induced by the resonators, while it has no influence at higher frequencies as compared to the uniform plate with no resonators (UNI). Note that at this point we are considering non-damped resonators (as opposed to the results previously shown in Fig. 4). The importance of damping the resonators will be made apparent below. The results from Fig. 7 are reasonable since the resonators have been tuned so that the bandgap suppresses the first plate mode, which is the one having more energy.

If we next have a look at the MSV of the MMABH plate (see Fig. 8), we observe that we basically get a

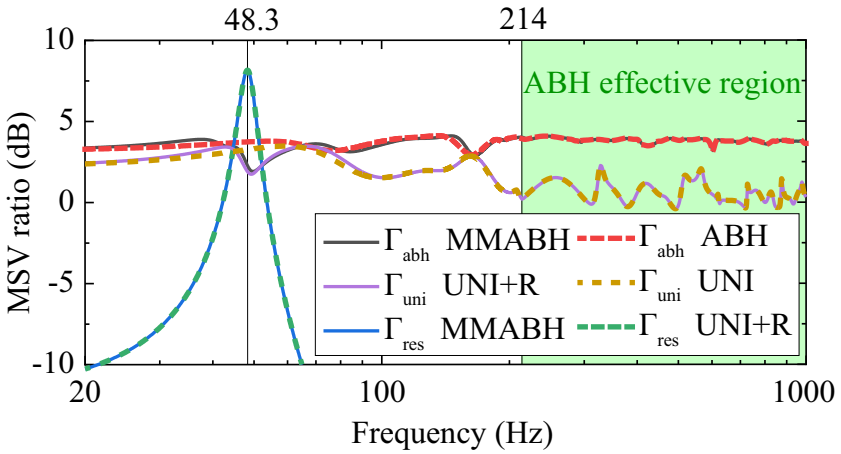

Figure 9: Mean square velocity (MSV) ratio for ABH, uniform, uniform with local resonators and MMABH plate. Γ_{abh} indicates the ratio between the MSV of the ABH portion and that of the total plate surface. Γ_{uni} stands for the ratio between the MSV of the circle $r < r_{\text{abh}}$ to the total MSV for a uniform plate. Γ_{res} represents the ratio between the MSV of the resonators to that of the plate surface.

combination of the results in Figs. 6 and 7. At the lower frequencies, the bandgap suppresses the first mode of the MMABH plate but other resonances still have very significant peak values. It is important to note that the bandgap also clearly manifests in this case despite the thickness of the ABH is not constant. This was not evident a priori, but somewhat expected from the analysis of the bandgap variation with thickness in Appendix A.2. For frequencies beyond the diameter cut-on frequency (214 Hz), the ABH effect clearly manifests in Fig. 8 and the MMABH experiences the substantial vibration reduction depicted in Fig. 6.

It appears from Fig. 8 that the coupling between the ABH effect and the local resonance is rather weak. To better assert this point and quantify the coupling between the two effects in the MMABH let us proceed as follows. On the one hand, for an ABH plate the ABH effect can be characterized trough $\Gamma_{\text{abh}} = \text{MSV}_{\text{abh}}/\text{MSV}_{\text{total}}$, which is the ratio between the MSV in the ABH area and the MSV of the total plate surface. Analogously and for comparison, in the case of a uniform plate we can compute $\Gamma_{\text{uni}} = \text{MSV}_{r\leq r_{\text{abh}}}/\text{MSV}_{\text{total}}$ as the ratio of the MSV within the circle $r \leq r_{\text{abh}}$ over that of the whole uniform

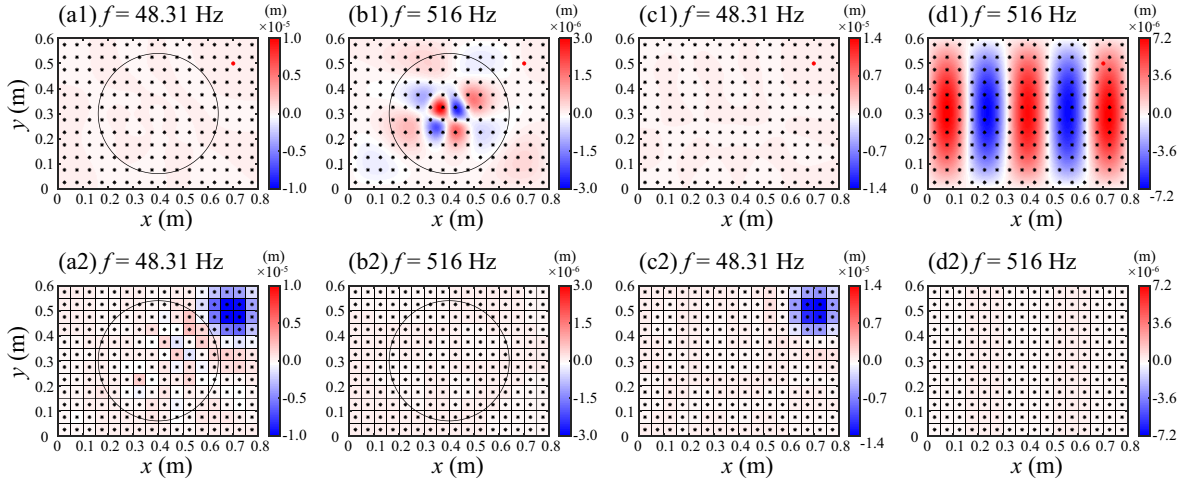

Figure 10: Forced vibration shapes of the ABH and UNI plates (first row) and the resonators (second row). Figures (a)-(b) represent the shapes of the MMABH plate, while figures (c)-(d) contains the shapes of the UNI plate with local resonators.

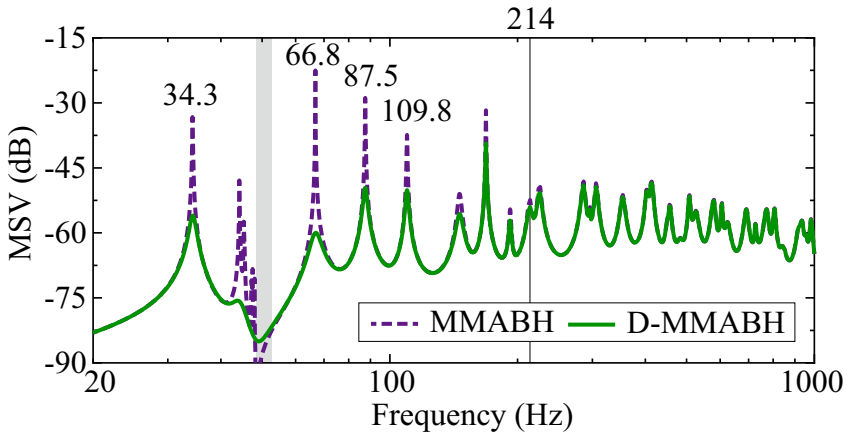

Figure 11: Influence of the damping of resonators on the MMABH plate's MSV.

surface. Given that strong vibration concentrates in the ABH region, it must happen that $\Gamma_{\text{abh}} > \Gamma_{\text{uni}}$ above the cut-on frequency. This is clearly observed in Fig. 9 if one compares the ratio Γ_{abh} of the ABH plate (red dashed line) with Γ_{uni} of the uniform plate (brown dashed line) beyond $f_{\text{cut-on}} = 214$ Hz. On the other hand, for a uniform plate with local resonators we could similarly define the ratio $\Gamma_{\text{res}} = \text{MSV}_{\text{res}}/\text{MSV}_{\text{total}}$ between the MSV of the resonators and that of the entire plate surface. As seen in Fig. 9, the ratio Γ_{res} (green dashed line) only dominates in the vicinity of 48.3 Hz and becomes negligible long before reaching the ABH cut-on frequency. This means that the two mechanisms, local resonance and ABH effect, occur in different frequency ranges, which is logical since the resonators have been tuned for low frequencies. Next, let us see what happens for the MMABH plate, where the two mechanisms become integrated. If we first compute Γ_{abh} for the MMABH plate (continuous black line) and compare it with Γ_{abh} of the ABH plate (red dashed line) no differences can be appreciated except for a slight dip close to 48.3 Hz for the former. Besides, if one adds resonators to the uniform plate one can observe that Γ_{uni} remains almost identical (purple continuous line versus brow dashed line) with, again, only a small variation near the resonant frequency. If we finally contrast Γ_{res} for the MMABH plate and the uniform plate with resonators (continuous blue line against green dashed line) no differences are observed. All in all, this means that the effects of the local resonators and the ABH indentation are weakly coupled in the MMABH plate. This is actually good news, as it could facilitate future metaplate designs for broadband vibration reduction.

To better understand the MMABH behavior, some forced vibration shapes have been calculated and plotted in Fig. 10, where the first row represents the ABH plate (Figs. 10a1 and 10b1) and the UNI one (Figs. 10c1 and 10d1). The second row contains the response of the resonators, which are connected to the plates at the locations indicated by the black asterisks. At $f = 48.31$ Hz (namely in the band gap), the resonators in the vicinity of the excitation point exhibit large vibrations while the ABH and UNI plates remain still (see Figs. 10a1 and 10a2, and Figs. 10c1 and 10c2). Nonetheless, at a higher frequency like $f = 516$ Hz, the plates dominate the total system vibration and the resonators barely move. Comparing Fig. 10b1 and Fig. 10d1 one can clearly appreciate the benefits of the ABH effect.

Tuning the resonators helps suppressing the first mode of the plate but has no effect on other plate resonances. In order to improve the low frequency performance of the MMABH not only at its first eigenomde but also at all other modes, an efficient strategy is that of damping the resonators (see e.g., [61–63]). For instance, if we allow the resonators to have some structural damping such that their stiffness becomes complex, $k_r(1 + \mathrm{i}\eta_r)$, with $\eta_r = 0.1$ being the loss factor, all resonant peaks get reduced. This is shown in Fig. 11, where we compare the MSV of the MMABH plate with damped resonators (D-MMABH) with the MMABH plate with non-damped resonators. As observed, the typical problem of ABHs at low-frequencies gets clearly mitigated when damping the resonators, offering a broadband vibration reduction that covers the whole frequency range. These results are in agreement with the previously shown behaviour of the plate

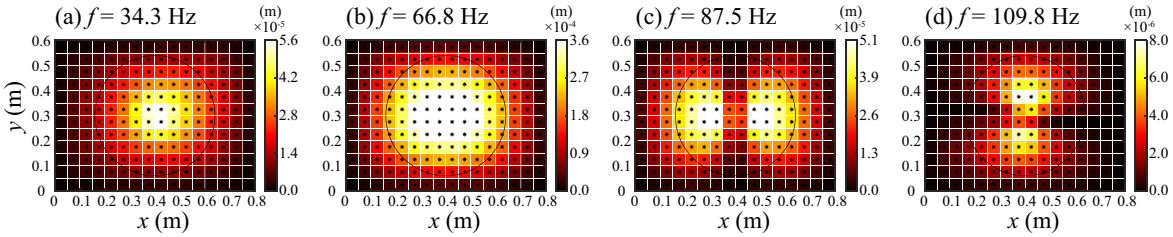

Figure 12: Displacement difference amplitude between the resonators and the plate at the connection points.

modal loss factors in Fig. 4.

To examine the damping effects of the resonators in some more detail, we have calculated and plotted the displacement difference between the resonators and the connection points on the damped MMABH plate in Fig. 12, for the frequencies $f = \{34.3, 66.8, 87.5, 109.36\}$ Hz highlighted in Fig. 11. Even though at these frequencies the resonators may have very limited vibration because they are far from 48.3 Hz, their influence is remarkable. The reason is that the plate has strong vibration values at these frequencies, so there is a large displacement difference between the plate and the resonators that positively correlates with the damping effect (because the potential energy in the spring is proportional to the displacement difference). As observed in Fig. 12, at $f = 66.8$ Hz the difference is the largest one (up to 3.6×10^{-4} m, see Fig. 12b), which corresponds to the biggest peak reduction in Fig. 11. Differences up to 5.6×10^{-5} m are achieved for $f = 34.3$ Hz (see Fig. 12a), followed by 5.1×10^{-5} m at $f = 87.5$ Hz (Fig. 12c) and 8.0×10^{-6} m at $f = 109.8$ Hz (Fig. 12d).

3.3. Influence of the lattice constant

To finish the analysis on the performance of the MMABH plate we will investigate the influence of the lattice constant on its MSV response to the point external excitation. In Appendix A.1 it has been shown that the lattice constant shows no influence on the bandgap analysis. That is, if one reduces the number of resonators keeping their total mass constant and adjusts the spring stiffness (to keep the resonant frequency at 48.3 Hz), the lattice constant augments but the bandgap remains almost unaltered. It is therefore worthwhile checking whether this is also the case for the simply supported MMABH plate. Fig. 13 confirms this point. The MSV values corresponding to the four different lattice constant values of $a = \{0.04, 0.05, 0.10, 0.20\}$ m present meaningless differences.

One may next wonder what would occur if we push the process to the limit in which a single resonator

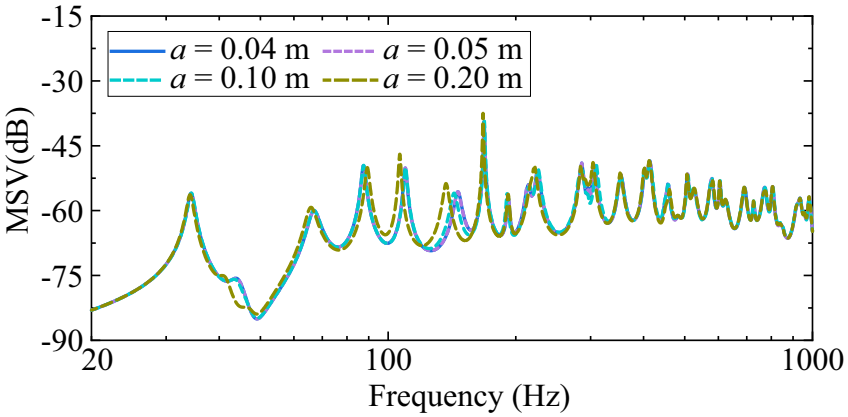

Figure 13: Influence of the lattice constant on the MMABH MVS when the total mass of the resonators is kept constant and their corresponding stiffness adjusted to have a resonant frequency of 48.3 Hz.

is placed at the center of the plate. It was shown in [46] that a single resonator with a large mass could suffice to reduce the vibration of the first eigenmode of a uniform plate. While this is certainly the case for a uniform plate (see Fig. 14a), the situation is more intricate for an ABH one. For the uniform plate, a single resonator can significantly suppress the first peak as observed in the purple line of Fig. 14a (see also the three first forced vibration shapes of the plate with a single resonator plotted in the figure). However, in this case the resonator acts as a dynamic vibration absorber (DVA) and no bandgap is formed as bandgaps are a consequence of imposing cell periodic boundary conditions. However, when we split, for instance, the big resonator into 4 smaller ones and distribute them on the plate surface, the peak reduction is then achieved thanks to the bandgap formation (see the brown line in the figure). The situation is more intricate for the ABH plate. As observed in Fig. 14b, if we add a single resonator the peak near 48.3 Hz is barely reduced (red line against black line) in contrast to what occurred for the uniform plate (compare also the forced vibrations for the ABH and uniform plates with a single resonator). The problem here is that the thickness at the center of the ABH is very small and reducing the first peak with a single resonator would require a non-trivial tuning process, which is deemed out of the scope of this paper. As opposed, when using 4 uniformly distributed resonators a significant reduction of the first peak is achieved thanks to bandgap formation.

Finally, let us note that in the the strategy followed in this work we have simply tuned the resonators to the plate first eigenmode and shown that if one properly dampers them the peaks of other eigenfrequencies substantially diminish too. Alternatives could have been followed too. For instance, in [46] an optimization process was followed to tune the parameters and locations of different resonators to suppress the first three modes of a uniform plate.

4. Conclusions

In this paper we have suggested the design of a metaplate (MMABH) that is able to suppress bending vibrations on a broadband spectrum. The MMABH combines the performance of the ABH effect at high frequencies with the bandgap formation at low frequencies, typical from locally resonant acoustic metamaterials. The MMABH consists of an ABH plate with attached periodic local resonators on its flat surface. The resonators are tuned to suppress the ABH plate first eigenmode and become damped to also reduce other low-frequency eigenmodes. To analyze the performance of the MMABH, a semi-analytical approach has been proposed, namely the GECMS, which integrates the GEM method to determine the ABH plate vibrations and a CMS approach to reduce the order of the model and connect the resonators to the plate. It has been shown that the proposed GECMS method is very efficient and accurate by comparison with FEM simulations.

In order to understand and design the MMABH, we have started analysing its modal behaviour. It has been shown that the modal loss factors (MLFs) of the MMABH are very high, compared to those of a uniform plate. Furthermore, the modal shapes of the MMABH plate have been carefully examined to see how the local resonators interact with the flexural motion of the ABH plate. Next, the forced vibration of the MMABH has been investigated, showing that the MMABH plate is able to provide broadband low mean square velocity (MSV), as compared to uniform and conventional ABH plates. Finally, we have shown that the lattice constant almost has no influence on the MSV response of the MMABH plate, provided one keeps the total mass of the resonators constant and properly adjusts their stiffness.

The significant broadband vibration reduction of the MMABH observed in this study suggests this design has also strong potential for diminishing sound radiation and that it could constitute a lightweight solution for improving transmission loss between dwellings (remember that the plate mass extracted for the ABH indentation has been used for the resonators). Future works will consider such aspects, as well the realization of experiments to see how the MMABH will behave in practical circumstances.

Acknowledgments

This work was supported by National Natural Science Foundation of China (grant number 52171323) and China Postdoctoral Science Foundation (grant number 2018M631194 and 2020T130533).

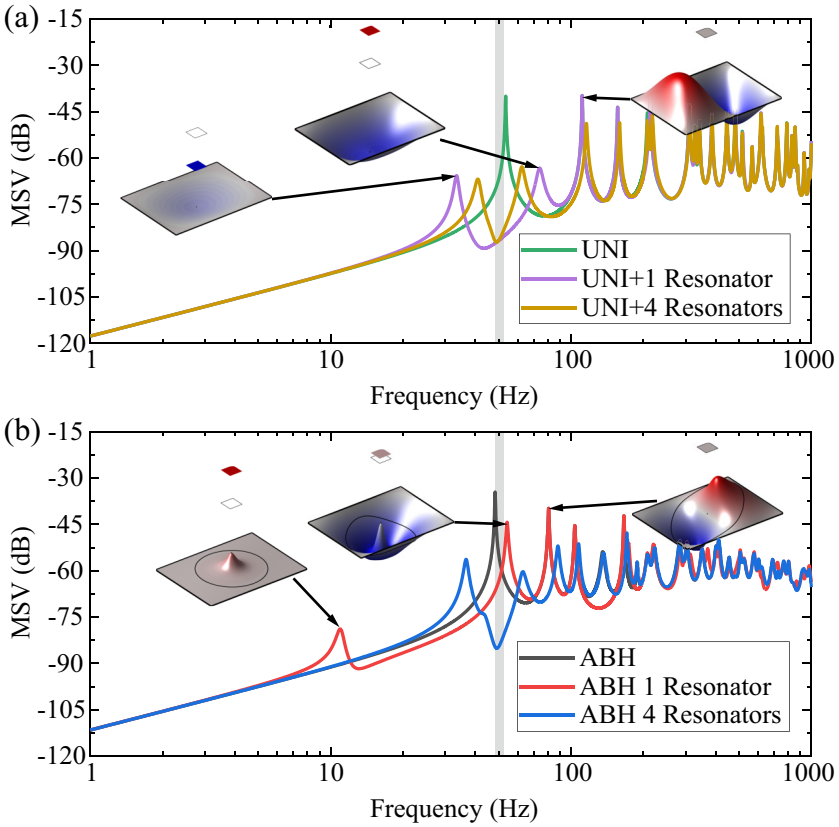

Figure 14: (a) Effects of placing 1 big resonator at the center of a uniform plate compared to that of placing 4 uniformly distributed resonators. (b) Effects of placing 1 big resonator at the center of an ABH plate compared to that of placing 4 uniformly distributed resonators. The first 3 forced vibration shapes of the uniform and ABH plates when adding 1 big resonator at their center have been included.

Appendix A. Band gaps of infinite periodic plates

Appendix A.1. The GECMS method for computing the dispersion curves of infinite periodic plates

In this appendix it will be shown how the essentials of the proposed GECMS method in section 2.2 can be adopted to compute the dispersion curves of an infinite uniform plate with locally attached resonators. Consider an infinite plate of constant thickness h having the unit cell represented in Fig. 1d. The resonators are linked at the cells center. Our initial objective is to determine the dispersion curves and bandgap formation in such a system. Let us first focus on the cell without resonator. The following Bloch-Floquet periodic boundary conditions must be satisfied at its boundaries,

$$w\left(-\frac{a}{2},y\right)=w\left(\frac{a}{2},y\right)\mathrm{e}^{-\mathrm{i}k_x a},\ w\left(x,-\frac{a}{2}\right)=w\left(x,\frac{a}{2}\right)\mathrm{e}^{-\mathrm{i}k_y a}, \tag{A.1}$$

$$\frac{\partial w}{\partial x}\left(-\frac{a}{2},y\right)=\frac{\partial w}{\partial x}\left(\frac{a}{2},y\right)\mathrm{e}^{-\mathrm{i}k_x a},\ \frac{\partial w}{\partial y}\left(x,-\frac{a}{2}\right)=\frac{\partial w}{\partial y}\left(x,\frac{a}{2}\right)\mathrm{e}^{-\mathrm{i}k_y a}, \tag{A.2}$$

$$\frac{\partial^2 w}{\partial x^2}\left(-\frac{a}{2},y\right)=\frac{\partial^2 w}{\partial x^2}\left(\frac{a}{2},y\right)\mathrm{e}^{-\mathrm{i}k_x a},\ \frac{\partial^2 w}{\partial y^2}\left(x,-\frac{a}{2}\right)=\frac{\partial^2 w}{\partial y^2}\left(x,\frac{a}{2}\right)\mathrm{e}^{-\mathrm{i}k_y a}, \tag{A.3}$$

$$\frac{\partial^3 w}{\partial x^3}\left(-\frac{a}{2},y\right)=-\frac{\partial^3 w}{\partial x^3}\left(\frac{a}{2},y\right)\mathrm{e}^{-\mathrm{i}k_x a},\ \frac{\partial^3 w}{\partial y^3}\left(x,-\frac{a}{2}\right)=-\frac{\partial^3 w}{\partial y^3}\left(x,\frac{a}{2}\right)\mathrm{e}^{-\mathrm{i}k_y a}. \tag{A.4}$$

It is to be noted that the Gaussian functions in Eq. (1) do not satisfy the above periodic conditions, unless they get modified for that purpose. An efficient way to do so was developed in [23, 25]. Hereafter, let us denote by χ_r the Gaussian functions fulfilling the periodicity in Eqs. (A.1)-(A.4) to distinguish them from χ in Eq. (1).

Using this new function basis, we can obtain the mass matrix for the unit cell as,

$$\boldsymbol{M}_p(k_x,k_y) = \rho_p h \int_{-a/2}^{a/2}\int_{-a/2}^{a/2} \boldsymbol{\chi}_r(k_x,k_y,x,y)\boldsymbol{\chi}_r^{\mathrm{H}}(k_x,k_y,x,y)\mathrm{d}x\mathrm{d}y, \tag{A.5}$$

and the stiffness matrix as,

$$\begin{aligned}\boldsymbol{K}_p(k_x,k_y) =& D\int_{-a/2}^{a/2}\int_{-a/2}^{a/2}\left[\frac{\partial^2\boldsymbol{\chi}_r}{\partial x^2}(k_x,k_y,x,y)\frac{\partial^2\boldsymbol{\chi}_r^{\mathrm{H}}}{\partial x^2}(k_x,k_y,x,y) + \frac{\partial^2\boldsymbol{\chi}_r}{\partial y^2}(k_x,k_y,x,y)\frac{\partial^2\boldsymbol{\chi}_r^{\mathrm{H}}}{\partial y^2}(k_x,k_y,x,y)\right.\\ &+\nu\frac{\partial^2\boldsymbol{\chi}_r}{\partial x^2}(k_x,k_y,x,y)\frac{\partial^2\boldsymbol{\chi}_r^{\mathrm{H}}}{\partial y^2}(k_x,k_y,x,y) + \nu\frac{\partial^2\boldsymbol{\chi}_r}{\partial y^2}(k_x,k_y,x,y)\frac{\partial^2\boldsymbol{\chi}_r^{\mathrm{H}}}{\partial x^2}(k_x,k_y,x,y)\\ &\left.+\ 2(1-\nu)\frac{\partial^2\boldsymbol{\chi}_r}{\partial x\partial y}(k_x,k_y,x,y)\frac{\partial^2\boldsymbol{\chi}_r^{\mathrm{H}}}{\partial y\partial x}(k_x,k_y,x,y)\right]\mathrm{d}x\mathrm{d}y.\end{aligned} \tag{A.6}$$

In Eqs. (A.5)-(A.6), the superscript $^{\mathrm{H}}$ represents the Hermitian (conjugate transpose) and $\boldsymbol{\chi}_r(k_x,k_y,x,y)$ is the new basis vector containing the above introduced functions χ_r.

From $\boldsymbol{M}_p(k_x,k_y)$ and $\boldsymbol{K}_p(k_x,k_y)$, the wavenumber depending eigenproblem of the plate unit cell turns to be

$$\left[\boldsymbol{K}_p(k_x,k_y) - \omega^2\boldsymbol{M}_p(k_x,k_y)\right]\hat{\boldsymbol{A}} = \boldsymbol{0}. \tag{A.7}$$

The solution to Eq. (A.7) provides the truncated mass-normalized modal matrix $\overline{\boldsymbol{P}} = [\overline{\boldsymbol{A}}_1, \overline{\boldsymbol{A}}_2, \overline{\boldsymbol{A}}_3, ..., \overline{\boldsymbol{A}}_i, ..., \overline{\boldsymbol{A}}_{\overline{N}}]$, with $\overline{N} \ll N$, from which we get the generalized mass and stiffness matrices,

$$\begin{aligned}\overline{\boldsymbol{M}}_p(k_x,k_y) &= \overline{\boldsymbol{P}}^{\top}\boldsymbol{M}_p(k_x,k_y)\overline{\boldsymbol{P}},\\ \overline{\boldsymbol{K}}_p(k_x,k_y) &= \overline{\boldsymbol{P}}^{\top}\boldsymbol{K}_p(k_x,k_y)\overline{\boldsymbol{P}}.\end{aligned} \tag{A.8}$$

Besides, projecting the weight coefficient into the modal space provides

$$\boldsymbol{a} = \overline{\boldsymbol{P}}\boldsymbol{\varepsilon}_p, \tag{A.9}$$

where $\boldsymbol{\varepsilon}_i$ are the vectors of modal participation factors. Considering Eq. (A.9), the kinetic energy of the plate unit cell reads,

$$T_p = \frac{1}{2}\dot{\boldsymbol{a}}^{\top}\boldsymbol{M}_p(k_x,k_y)\dot{\boldsymbol{a}} = \frac{1}{2}(\overline{\boldsymbol{P}}\dot{\boldsymbol{\varepsilon}}_p)^{\top}\boldsymbol{M}_p(k_x,k_y)(\overline{\boldsymbol{P}}\dot{\boldsymbol{\varepsilon}}_p) = \frac{1}{2}\dot{\boldsymbol{\varepsilon}}_p^{\top}\left[\overline{\boldsymbol{P}}^{\top}\boldsymbol{M}_p(k_x,k_y)\overline{\boldsymbol{P}}\right]\dot{\boldsymbol{\varepsilon}}_p \equiv \frac{1}{2}\dot{\boldsymbol{\varepsilon}}_p^{\top}\overline{\boldsymbol{M}}_p(k_x,k_y)\dot{\boldsymbol{\varepsilon}}_p, \tag{A.10}$$

where in the last equality we have defined the reduced mass matrix of the system (which is the identity matrix as we are using mass-normalized eigenvectors).

At this point, we can follow analogous steps to those in section 2.2 and include the influence of the resonator on the unit cell. The kinetic energy of the resonator is given by,

$$T_r = \frac{1}{2}\dot{w}_r\Delta M_r\dot{w}_r = \frac{1}{2}\dot{\overline{w}}_r\dot{\overline{w}}_r, \tag{A.11}$$

where $\overline{w}_r = w_r/\sqrt{\Delta M_r}$. Therefore, the total kinetic energy of the unit cell (plate plus resonator) in Fig. 1d

is nothing but the summation,

$$\begin{aligned} T &= T_p + T_r \\ &= \frac{1}{2}\dot{\boldsymbol{\varepsilon}}_p^\top \overline{\boldsymbol{M}}_p(k_x,k_y)\dot{\boldsymbol{\varepsilon}}_p + \frac{1}{2}\dot{\overline{w}}_r\dot{\overline{w}}_r \\ &= \frac{1}{2}\begin{bmatrix} \dot{\boldsymbol{\varepsilon}}_p \\ \dot{\overline{w}}_r \end{bmatrix}^\top \begin{bmatrix} \overline{\boldsymbol{M}}_p(k_x,k_y) & \mathbf{0} \\ \mathbf{0} & 1 \end{bmatrix} \begin{bmatrix} \dot{\boldsymbol{\varepsilon}}_p \\ \dot{\overline{w}}_r \end{bmatrix} \\ &\equiv \frac{1}{2}\dot{\boldsymbol{\varepsilon}}^\top \overline{\boldsymbol{M}}(k_x,k_y)\dot{\boldsymbol{\varepsilon}}. \end{aligned} \tag{A.12}$$

Likewise, the potential energy of the plate unit cell in modal space turns to be,

$$V_p = \frac{1}{2}\boldsymbol{a}^\top \boldsymbol{K}_p(k_x,k_y)\boldsymbol{a} = \frac{1}{2}(\overline{\boldsymbol{P}}\boldsymbol{\varepsilon}_p)^\top \boldsymbol{K}_p(k_x,k_y)(\overline{\boldsymbol{P}}\boldsymbol{\varepsilon}_p) = \frac{1}{2}\boldsymbol{\varepsilon}_p^\top \left[\overline{\boldsymbol{P}}^\top \boldsymbol{K}_p(k_x,k_y)\overline{\boldsymbol{P}}\right]\boldsymbol{\varepsilon}_p \equiv \frac{1}{2}\boldsymbol{\varepsilon}_p^\top \overline{\boldsymbol{K}}_p(k_x,k_y)\boldsymbol{\varepsilon}_p, \tag{A.13}$$

with $\overline{\boldsymbol{K}}_p$ being the normalized and truncated stiffness matrix, which is diagonal. The potential energy stored in the resonator spring can be expressed as

$$\begin{aligned} V_r &= \frac{1}{2}k\left[w_p(k_x,k_y,x_c,y_c) - w_r\right]^2 \\ &= \frac{1}{2}k\left[w_p^2(k_x,k_y,x_c,y_c) - w_p(k_x,k_y,x_c,y_c)w_r - w_r w_p(k_x,k_y,x_c,y_c) + w_r^2\right] \\ &= \frac{1}{2}\begin{bmatrix} \boldsymbol{\varepsilon}_p \\ \overline{w}_r \end{bmatrix}^\top \left(\begin{bmatrix} \overline{\boldsymbol{P}} & \mathbf{0} \\ \mathbf{0} & 1 \end{bmatrix}^\top \begin{bmatrix} k\boldsymbol{\chi}_r\boldsymbol{\chi}_r^{\mathrm{H}} & -k\boldsymbol{\chi}_r \\ -k\boldsymbol{\chi}_r^{\mathrm{H}} & \omega_r^2 \end{bmatrix} \begin{bmatrix} \overline{\boldsymbol{P}} & \mathbf{0} \\ \mathbf{0} & 1 \end{bmatrix} \right) \begin{bmatrix} \boldsymbol{\varepsilon}_p \\ \overline{w}_r \end{bmatrix} \\ &\equiv \frac{1}{2}\boldsymbol{\varepsilon}^\top \boldsymbol{K}_r(k_x,k_y)\boldsymbol{\varepsilon}, \end{aligned} \tag{A.14}$$

where $\boldsymbol{\chi}_r = \boldsymbol{\chi}_r(k_x,k_y,x_c,y_c)$. From Eqs. (A.13) and (A.14) the total potential energy for the unit cell in Fig. 1d becomes,

$$\begin{aligned} V &= V_p + V_r \\ &= \frac{1}{2}\boldsymbol{\varepsilon}_p^\top \overline{\boldsymbol{K}}_p(k_x,k_y)\boldsymbol{\varepsilon}_p + \frac{1}{2}\boldsymbol{\varepsilon}^\top \boldsymbol{K}_r\boldsymbol{\varepsilon} \\ &= \frac{1}{2}\boldsymbol{\varepsilon}^\top \left(\begin{bmatrix} \overline{\boldsymbol{K}}_p(k_x,k_y) & \mathbf{0} \\ \mathbf{0} & 0 \end{bmatrix} + \boldsymbol{K}_r \right)\boldsymbol{\varepsilon} \\ &\equiv \frac{1}{2}\boldsymbol{\varepsilon}^\top \overline{\boldsymbol{K}}(k_x,k_y)\boldsymbol{\varepsilon}. \end{aligned} \tag{A.15}$$

Observe that in the last lines of Eqs. (A.12) and (A.15) we have introduced the total mass and stiffness matrices for a unit cell in the wavenumber domain.

Finally, applying the Euler-Lagrange equations to Eqs. (A.12)-(A.15) and assuming $\boldsymbol{\varepsilon} = \hat{\boldsymbol{\varepsilon}}\exp(\mathrm{i}\omega t)$, we get the eigenvalue problem for the plate periodic unit cell with resonator,

$$\left[\overline{\boldsymbol{K}}(k_x,k_y) - \omega^2\overline{\boldsymbol{M}}(k_x,k_y)\right]\hat{\boldsymbol{\varepsilon}} = \mathbf{0}. \tag{A.16}$$

In the Brillouin zone (BZ), the wavenumber can be restricted to $k_x \times k_y = [-\frac{\pi}{a}, \frac{\pi}{a}] \times [-\frac{\pi}{a}, \frac{\pi}{a}]$. From Eq. (A.16), we can compute the dispersion curves as usual, by sectioning the BZ and sweeping the wavenumber along the edges ($\Gamma - X - M - \Gamma$) of the irreducible Brillouin zone (IBZ).

Appendix A.2. Dispersion curves and bandgap analysis of the infinite periodic uniform plate with resonators

In Fig. A.1, we show the dispersion curves of the infinite periodic lattice respectively computed with the GECMS (red curve) and with FEM (blue dots), using the unit cell parameters in Table 1. The matching

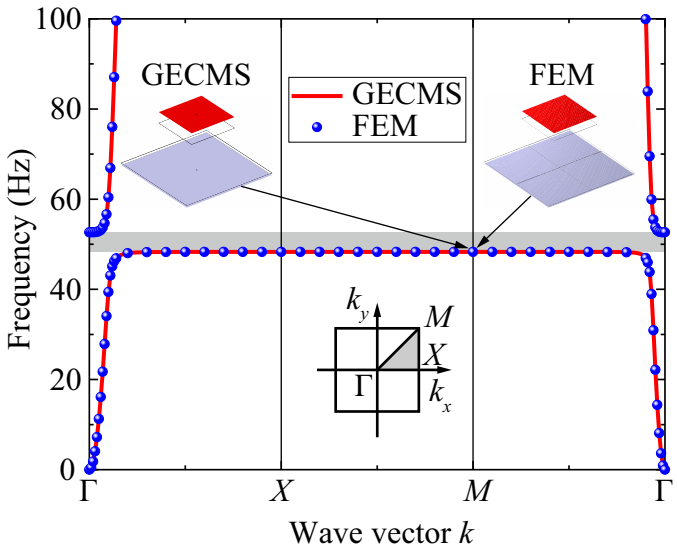

Figure A.1: Dispersion curves within 100 Hz resulted by the GECMS and FEM. Note the eigenmodes at the lower bound of the band gap calculated with SCMS and FEM have been also included in the figure.

is remarkable, confirming again the validity of the GECMS. It can also be observed in the figure that a bandgap appears between 48.2995 Hz and 52.6553 Hz. An eigenmode at the lower bound of the band gap has been also computed with the GECMS and FEM and plotted in Fig. A.1 for comparison. There, the bottom layer represents the plate and the upper one the resonator. Both methods exhibit almost identical results, showing that, at this frequency, the plate stands still while the resonator strongly vibrates as one could expect (the resonator was tuned for that purpose).

Having confirmed the reliability of the GECMS for eigenproblems like Eq. (A.16), we will next analyze the influence of some parameters on the bandgap formation. Remember that our final goal in this study is to improve the performance of the ABH plate at low frequencies, for which one could presume the need of wide

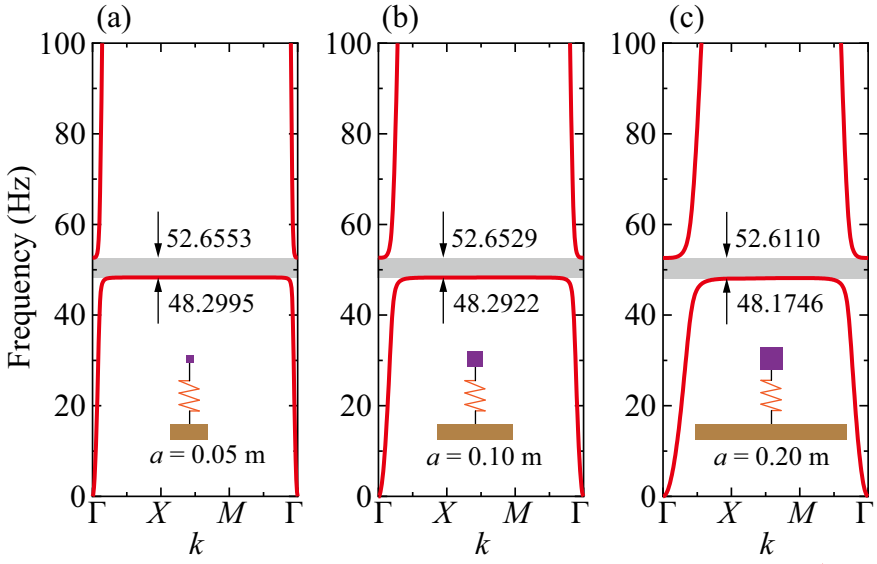

Figure A.2: Influence of the lattice constant constant on bandgap formation.

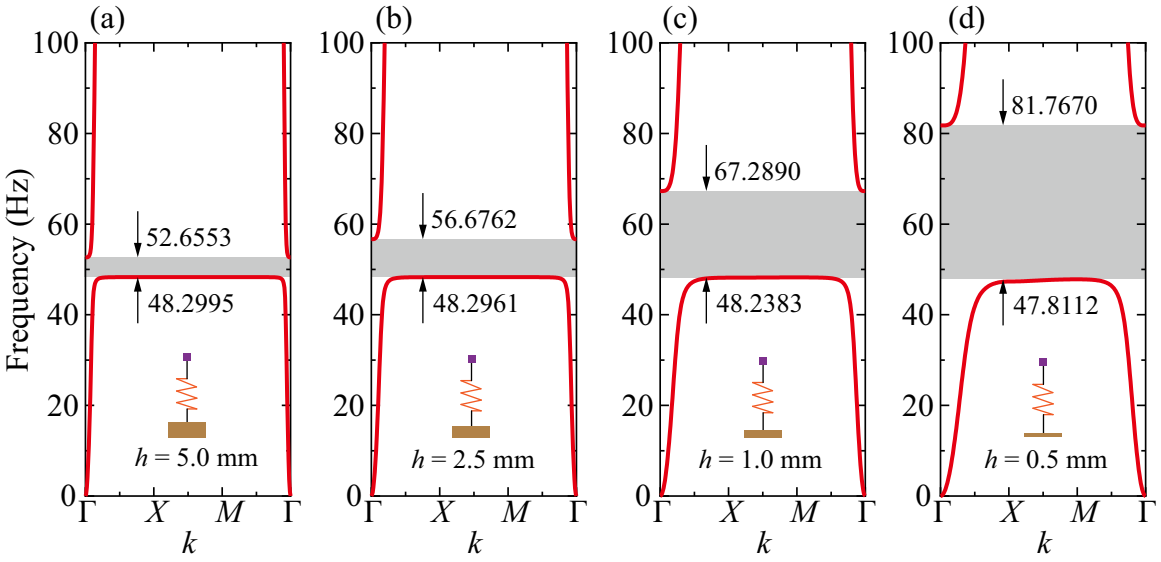

Figure A.3: Influence of the unit cell plate thickness on bandgap formation.

bandgaps. Unfortunately, those produced by local resonances are usually narrow, but we get to that point latter on, in the main text. We start checking how the distribution of the resonators affects the bandgap in Fig. A.1. As said at the beginning of section 2.3, the total mass $\Delta M = 3.5286$ kg is uniformly assigned to $16 \times 12 = 192 \equiv N_r$ resonators, each one having mass $\Delta M_r = 0.0184$ kg and a lattice constant $a = 0.05$ m. However, other strategies could have been adopted. For instance, we could have kept the total mass fixed but only attach $8 \times 6 = 48$ resonators to the plate with mass $\Delta M_r = 0.0735$ kg and lattice constant $a = 0.10$ m, or we could have simply used $4 \times 3 = 12$ resonators with $\Delta M_r = 0.2940$ kg and $a = 0.20$ m. To retain the same resonant frequency, $f_r = 48.3$ Hz, in both cases, the spring stiffness shall be modified to $k_r = 6769.3$ N/m and $k_r = 27077$ N/m, respectively. The dispersion curves and bandgap values of these three options have been plotted in Fig. A.2. For $a = 0.05$ m the band gap comprises the interval $[48.2995, 52.6553]$ Hz, while for $a = 0.10$ m it is given by $[48.2922, 52.6529]$ Hz, and for $a = 0.20$ m by $[48.1746, 52.6110]$ Hz. As seen, changes are almost negligible from one design to another, which is reasonable because the total mass of the resonators is identical. Therefore, the current results seem to indicate that there is no need to design very dense and small resonators in infinite periodic structures to achieve a band gap for a fixed value of the total mass. In practice, however, a structure is always finite and the periodicity is ruined if one chooses a few resonators with large masses. This may cause wave leakage (see e.g., [23]). As opposed, when very small lattice constants are considered the periodicity is still relevant in finite domains (e.g., $L_x \times L_y = 0.8 \times 0.6$ m^2 in our case), but the manufacturing complexity may be demanding. To summarize, if the total mass is fixed, choosing a given lattice constant is a trade off between achieving periodicity and manufacturing difficulties.

Finally, it is worth analyzing the effects of the plate thickness on bandgaps, given that in the case of an ABH plate the thickness will not be constant (see Figs. 1a and 1b). In Fig. A.3 we consider four different thicknesses, $h = \{5.0, 2.5, 1.0, 0.5\}$ mm, which vary between the limiting values found in the ABH of the main text, namely $h_{\text{uni}} = 5$ mm and $h_c = 0.5$ mm. It is observed in the figure that as the thickness h decreases, the upper bound of the band gap increases from 52.6553 Hz to 81.7670 Hz, whereas the lower bound remains almost unaltered (it only decreases from 48.2995 Hz to 47.8112 Hz). This behavior can be attributed to the increase in relative added mass when the plate thickness diminishes. This result suggests that the ABH profile may help broadening the bandgaps, which will benefit vibration reduction (although the herein assumed periodicity conditions do not apply to the ABH).

References

[1] A. Pelat, F. Gautier, S. C. Conlon, F. Semperlotti, The acoustic black hole: A review of theory and applications, J. Sound Vib. 476 (2020) 115316.

[2] E. P. Bowyer, D. J. OBoy, V. V. Krylov, J. L. Horner, Effect of geometrical and material imperfections on damping flexural vibrations in plates with attached wedges of power law profile 73 (2012) 514–523.

[3] D. J. OBoy, V. V. Krylov, V. Kralovic, Damping of flexural vibrations in rectangular plates using the acoustic black hole effect, J. Sound Vib. 329 (2010) 4672–4688.

[4] J. Deng, O. Guasch, L. Zheng, T. Song, Y. Cao, Semi-analytical model of an acoustic black hole piezoelectric bimorph cantilever for energy harvesting, J. Sound Vib. 494 (2021) 115790.

[5] V. V. Krylov, Propagation of plate bending waves in the vicinity of one-and two-dimensional acoustic black holes (2007).

[6] S. Conlon, J. Fahnline, F. Semperlotti, Numerical analysis of the vibroacoustic properties of plates with embedded grids of acoustic black holes, J. Acoust. Soc. Am. 137 (2015) 447–457.

[7] D. J. OBoy, E. P. Bowyer, V. V. Krylov, Point mobility of a cylindrical plate incorporating a tapered hole of power-law profile, J. Acoust. Soc. Am. 129 (2011) 3475–3482.

[8] J. Deng, O. Guasch, L. Maxit, L. Zheng, Transmission loss of plates with multiple embedded acoustic black holes using statistical modal energy distribution analysis, Mech. Syst. Signal Pr. 150 (2021) 107262.

[9] D. J. OBoy, V. V. Krylov, Vibration of a rectangular plate with a central power-law profiled groove by the RayleighRitz method, Appl. Acoust. 104 (2016) 24–32.

[10] J. Y. Lee, W. Jeon, Vibration damping using a spiral acoustic black hole, J. Acoust. Soc. Am. 141 (2017) 1437–1445.

[11] S. Park, M. Kim, W. Jeon, Experimental validation of vibration damping using an Archimedean spiral acoustic black hole, J. Sound Vib. 459 (2019) 114838.

[12] L. Tang, L. Cheng, Ultrawide band gaps in beams with double-leaf acoustic black hole indentations, J. Acoust. Soc. Am. 142 (2017) 2802–2807.

[13] J. Deng, O. Guasch, L. Zheng, A semi-analytical method for characterizing vibrations in circular beams with embedded acoustic black holes, J. Sound Vib. 476 (2020) 115307.

[14] V. Georgiev, J. Cuenca, F. Gautier, L. Simon, V. Krylov, Damping of structural vibrations in beams and elliptical plates using the acoustic black hole effect, J. Sound Vib. 330 (2011) 2497–2508.

[15] L. Tang, L. Cheng, Impaired sound radiation in plates with periodic tunneled Acoustic Black Holes, Mech. Syst. Signal Pr. 135 (2020) 106410.

[16] J. Deng, O. Guasch, L. Zheng, Ring-shaped acoustic black holes for broadband vibration isolation in plates, J. Sound Vib. 458 (2019) 109–122.

[17] J. Deng, L. Zheng, Noise reduction via three types of acoustic black holes, Mech. Syst. Signal Pr. 165 (2022) 108323.

[18] J. Deng, O. Guasch, L. Maxit, L. Zheng, Reduction of Bloch-Floquet bending waves via annular acoustic black holes in periodically supported cylindrical shell structures, Appl. Acoust. 169 (2020) 107424.

[19] J. Deng, O. Guasch, L. Maxit, L. Zheng, Vibration of cylindrical shells with embedded annular acoustic black holes using the Rayleigh-Ritz method with Gaussian basis functions, Mech. Syst. Signal Pr. 150 (2021) 107225.

[20] J. Deng, O. Guasch, L. Maxit, L. Zheng, Annular acoustic black holes to reduce sound radiation from cylindrical shells, Mech. Syst. Signal Pr. 158 (2021) 107722.

[21] L. Tang, L. Cheng, K. Chen, Complete sub-wavelength flexural wave band gaps in plates with periodic acoustic black holes, J. Sound Vib. 502 (2021) 116102.

[22] N. Gao, X. Guo, J. Deng, B. Cheng, H. Hou, Elastic wave modulation of double-leaf ABH beam embedded mass oscillator, Appl. Acoust. 173 (2021) 107694.

[23] J. Deng, L. Zheng, N. Gao, Broad band gaps for flexural wave manipulation in plates with embedded periodic strip acoustic black holes, Int. J. Solids Struct. 224 (2021) 111043.

[24] J. Deng, O. Guasch, L. Zheng, Elliptical acoustic black holes for flexural wave lensing in plates, Appl. Acoust. 174 (2021) 107744.

[25] J. Deng, O. Guasch, L. Zheng, Reconstructed Gaussian basis to characterize flexural wave collimation in plates with periodic arrays of annular acoustic black holes, Int. J. Mech. Sci. 194 (2021) 106179.

[26] J. Deng, L. Zheng, O. Guasch, H. Wu, P. Zeng, Y. Zuo, Gaussian expansion for the vibration analysis of plates with multiple acoustic black holes indentations, Mech. Syst. Signal Pr. 131 (2019) 317–334.

[27] W. Huang, C. Tao, H. Ji, J. Qiu, Enhancement of wave energy dissipation in two-dimensional acoustic black hole by simultaneous optimization of profile and damping layer, J. Sound Vib. 491 (2021) 115764.

[28] L. Tang, L. Cheng, Enhanced acoustic black hole effect in beams with a modified thickness profile and extended platform, J. Sound Vib. 391 (2017) 116–126.

[29] C. A. McCormick, M. R. Shepherd, Design optimization of three styles of acoustic black hole vibration absorbers, J. Acoust. Soc. Am. 145 (2019) 1823–1824.

[30] C. A. McCormick, M. R. Shepherd, Optimization of an acoustic black hole vibration absorber at the end of a cantilever beam, J. Acoust. Soc. Am. 145 (2019) EL593–EL597.

[31] M. R. Shepherd, P. A. Feurtado, S. C. Conlon, Multi-objective optimization of acoustic black hole vibration absorbers, J. Acoust. Soc. Am. 140 (2016) EL227–EL230.

[32] M. He, Q. Ding, Data-driven optimization of the periodic beam with multiple acoustic black holes, J. Sound Vib. 493 (2021) 115816.

[33] V. Denis, A. Pelat, C. Touzé, F. Gautier, Improvement of the acoustic black hole effect by using energy transfer due to geometric nonlinearity, Int. J. Non Linear Mech. 94 (2017) 134–145.

[34] V. E. Gusev, C. Ni, A. Lomonosov, Z. Shen, Propagation of flexural waves in inhomogeneous plates exhibiting hysteretic nonlinearity: Nonlinear acoustic black holes, Ultrasonics 61 (2015) 126–135.
[35] H. Li, C. Touzé, A. Pelat, F. Gautier, X. Kong, A vibro-impact acoustic black hole for passive damping of flexural beam vibrations, J. Sound Vib. 450 (2019) 28–46.
[36] H. Li, C. Touzé, F. Gautier, A. Pelat, Linear and nonlinear dynamics of a plate with acoustic black hole, geometric and contact nonlinearity for vibration mitigation, J. Sound Vib. 508 (2021) 116206.
[37] H. Li, M. Scail-Graud, A. Pelat, F. Gautier, C. Touzé, Experimental evidence of energy transfer and vibration mitigation in a vibro-impact acoustic black hole, Appl. Acoust. 182 (2021) 108168.
[38] W. Huang, H. Zhang, D. J. Inman, J. Qiu, C. E. Cesnik, H. Ji, Low reflection effect by 3D printed functionally graded acoustic black holes, J. Sound Vib. 450 (2019) 96–108.
[39] L. Zhao, Low-frequency vibration reduction using a sandwich plate with periodically embedded acoustic black holes, J. Sound Vib. 441 (2019) 165–171.
[40] N. Gao, Z. Wei, R. Zhang, H. Hou, Low-frequency elastic wave attenuation in a composite acoustic black hole beam, Appl. Acoust. 154 (2019) 68–76.
[41] T. Zhou, L. Cheng, A resonant beam damper tailored with acoustic black hole features for broadband vibration reduction, J. Sound Vib. 430 (2018) 174–184.
[42] H. Ji, N. Wang, C. Zhang, X. Wang, L. Cheng, J. Qiu, A vibration absorber based on two-dimensional acoustic black holes, J. Sound Vib. 500 (2021) 116024.
[43] J. Leng, V. Romero-Garca, F. Gautier, A. Pelat, R. Pic, J.-P. Groby, Optimal absorption of flexural energy in thin plates by critically coupling a locally resonant grating, Wave Random Complex 0 (2021) 1–23.
[44] V. Romero-García, G. Theocharis, O. Richoux, V. Pagneux, Use of complex frequency plane to design broadband and sub-wavelength absorbers, J. Acoust. Soc. Am. 139 (2016) 3395–3403.
[45] J. Leng, V. Romero-García, A. Pelat, R. Pic, J.-P. Groby, F. Gautier, Interpretation of the acoustic black hole effect based on the concept of critical coupling, J. Sound Vib. 471 (2020) 115199.
[46] X. Zhu, Z. Chen, Y. Jiao, Optimizations of distributed dynamic vibration absorbers for suppressing vibrations in plates, J. Low Freq. Noise V. A. 37 (2018) 1188–1200.
[47] L. Tang, N. Gao, J. Xu, K. Chen, L. Cheng, A light-weight periodic plate with embedded acoustic black holes and bandgaps for broadband sound radiation reduction, J. Acoust. Soc. Am. 150 (2021) 3532–3543.
[48] S. Nair, M. Jokar, F. Semperlotti, Nonlocal acoustic black hole metastructures: Achieving broadband and low frequency passive vibration attenuation, Mech. Syst. Signal Pr. 169 (2022) 108716.
[49] Z. Liu, X. Zhang, Y. Mao, Y. Y. Zhu, Z. Yang, C. T. Chan, P. Sheng, Locally resonant sonic materials, Science 289 (2000) 1734–1736.
[50] H. Huang, C. Sun, Wave attenuation mechanism in an acoustic metamaterial with negative effective mass density, New J. Phys. 11 (2009) 013003.
[51] P. Gao, A. Climente, J. Sánchez-Dehesa, L. Wu, Single-phase metamaterial plates for broadband vibration suppression at low frequencies, J. Sound Vib. 444 (2019) 108–126.
[52] F. Pires, C. Claeys, E. Deckers, W. Desmet, The impact of resonant additions footprint on the stop band behavior of 1d locally resonant metamaterial realizations, J. Sound Vib. 491 (2021) 115705.
[53] Z. Xiao, P. Gao, D. Wang, X. He, L. Wu, Ventilated metamaterials for broadband sound insulation and tunable transmission at low frequency, Extreme Mech. Lett. 46 (2021) 101348.
[54] N. de Melo Filho, L. Van Belle, C. Claeys, E. Deckers, W. Desmet, Dynamic mass based sound transmission loss prediction of vibro-acoustic metamaterial double panels applied to the mass-air-mass resonance, J. Sound Vib. 442 (2019) 28–44.
[55] L. Van Belle, C. Claeys, E. Deckers, W. Desmet, The impact of damping on the sound transmission loss of locally resonant metamaterial plates, J. Sound Vib. 461 (2019) 114909.
[56] A. Climente, P. Gao, L. Wu, J. Sánchez-Dehesa, Scattering of flexural waves from an n-beam resonator in a thin plate, J. Acoust. Soc. Am. 142 (2017) 3205–3215.
[57] P. Gao, A. Climente, J. Sánchez-Dehesa, L. Wu, Theoretical study of platonic crystals with periodically structured n-beam resonators, J. Appl. Phys. 123 (2018) 091707.
[58] C. Liu, J. Wu, Z. Yang, F. Ma, Ultra-broadband acoustic absorption of a thin microperforated panel metamaterial with multi-order resonance, Compos. Struct. 246 (2020) 112366.
[59] D. Roca, J. Cante, O. Lloberas-Valls, T. Pàmies, J. Oliver, Multiresonant Layered Acoustic Metamaterial (MLAM) solution for broadband low-frequency noise attenuation through double-peak sound transmission loss response, Extreme Mech. Lett. 47 (2021) 101368.
[60] H. H. Huang, C. T. Sun, Wave attenuation mechanism in an acoustic metamaterial with negative effective mass density, New J. Phys. 11 (2009) 013003.
[61] H. Peng, P. Frank Pai, Acoustic metamaterial plates for elastic wave absorption and structural vibration suppression, Int. J. Mech. Sci. 89 (2014) 350–361.
[62] Y. Xiao, J. Wen, X. Wen, Broadband locally resonant beams containing multiple periodic arrays of attached resonators, Phys. Lett. A 376 (2012) 1384–1390.
[63] Q. Qin, M. Sheng, Z. Guo, Low-frequency vibration and radiation performance of a locally resonant plate attached with periodic multiple resonators, Appl. Sci. 10 (2020) 2843.
[64] J. Deng, L. Zheng, P. Zeng, Y. Zuo, O. Guasch, Passive constrained viscoelastic layers to improve the efficiency of truncated acoustic black holes in beams, Mech. Syst. Signal Pr. 118 (2019) 461–476.
[65] L. Tang, L. Cheng, H. Ji, J. Qiu, Characterization of acoustic black hole effect using a one-dimensional fully-coupled and wavelet-decomposed semi-analytical model, J. Sound Vib. 374 (2016) 172–184.